Available online at www.sciencedirect.com
ScienceDirect
Journal of Computational Physics 225 (2007) 1961–1984
JOURNAL OF COMPUTATIONAL PHYSICS
www.elsevier.com/locate/jcp

Discontinuous Galerkin methods with plane waves for time-harmonic problems

Gwénaël Gabard

Institute of Sound and Vibration Research, University of Southampton, Southampton, SO17 1BJ, United Kingdom

Received 4 October 2006; received in revised form 27 February 2007; accepted 28 February 2007
Available online 13 March 2007

Abstract

A general framework for discontinuous Galerkin methods in the frequency domain with numerical flux is presented. The main feature of the method is the use of plane waves instead of polynomials to approximate the solution in each element. The method is formulated for a general system of linear hyperbolic equations and is applied to problems of aeroacoustic propagation by solving the two-dimensional linearized Euler equations. It is found that the method requires only a small number of elements per wavelength to obtain accurate solutions and that it is more efficient than high-order DRP schemes. In addition, the conditioning of the method is found to be high but not critical in practice. It is shown that the Ultra-Weak Variational Formulation is in fact a subset of the present discontinuous Galerkin method. A special extension of the method is devised in order to deal with singular solutions generated by point sources like monopoles or dipoles. Aeroacoustic problems with non-uniform flows are also considered and results are presented for the sound radiated from a two-dimensional jet.

Keywords: Discontinuous Galerkin methods; Plane wave; Aeroacoustics

1. Introduction

Prompted by the realization of the limitation of standard finite element methods, current developments in numerical methods for wave propagation tend to move beyond the standard continuous polynomial interpolation techniques. It has been recognized that for high frequencies, the pollution error in standard finite element models can become large and as a consequence very fine meshes are required to obtained accurate solutions [1]. This is due to the fact that the numerical error on the wavenumber (or equivalently on the phase speed) is solely controlled by the number of nodes per wavelength. At high frequencies waves can propagate over many wavelengths within the computational domain. A consequence is that the error on the phase is allowed to build up significantly over long distances. This accumulation process results in large numerical errors that can only be alleviated by the use of meshes with much higher resolution than that dictated by

E-mail address: gabard@soton.ac.uk

0021-9991/$ - see front matter
doi:10.1016/j.jcp.2007.02.030

the standard practice of keeping the number of nodes per wavelength constant (8 or 10 nodes per wavelength are common rules-of-thumb used with standard finite elements for Helmholtz problems).

Various avenues have been explored to remedy this shortcoming and one can distinguish between two, more or less distinct, approaches.

On the one hand, spectral methods take advantage of the superior interpolation properties of various family of functions compared to standard finite element shape functions. Fourier series and Tchebychev polynomials are common examples of shape functions used in spectral methods. High-order polynomials can also be used such as Lagrange and Hermite polynomials. Discontinuous Galerkin methods are commonly considered as spectral methods since the solution is generally interpolated using high-order polynomials [2] although non-polynomial bases have been recently considered for time-dependent problems [3]. A general overview of spectral methods can be found in [4].

On the other hand, 'physics-based' methods offer a way to include more *a priori* information on the physics of the problem into the numerical model. Whereas spectral methods focus on improving the mathematical property of approximability of functional spaces, physics-based methods aim at including key physical properties of the exact solutions into the numerical models (such as the dispersion properties for wave propagation problems or the discontinuous nature of the solutions for problems of crack propagation in elastic solids). This is achieved by using local solutions of the problem at hand to devise the numerical discretization of the global solution. One possibility is to use Green's functions to interpolate the solution. For instance, Caruthers et al. devised a Green Function Discretization (GFD) scheme for Helmholtz problems [5,6]. More common is the use of plane waves to interpolate the solution. With the partition of unity method (PUM) developed by Babuška and Melenk, the standard finite element shape functions are multiplied by a set of plane waves, thus preserving the conformity of the numerical model [7–9]. With the discontinuous enrichment method (DEM), the standard continuous shape functions are complemented with a set of plane waves in each element [10,11]. These additional shape functions being discontinuous across element boundaries, continuity is enforced by means of Lagrange multipliers. When the continuous shape functions are removed, the DEM reduces to a discontinuous Galerkin method with Lagrange multipliers [12,13]. Another physics-based numerical method is the ultra-weak variational formulation (UWVF) whereby the solution is described in each element by a set of plane waves [14–21]. Continuity between elements is weakly imposed using continuity conditions originating from domain decomposition methods. Monk and Wang followed a similar approach to the UWVF but used a least-square formulation to impose continuity between elements [22]. Capdeville has recently developed a family of finite difference schemes by means of a local plane wave reconstruction of the solution in order to adapt the upstream direction of the finite difference stencils [23,24]. Compared to standard finite element methods, all the physics-based methods cited above yield significant improvements in terms of accuracy for a fixed number of degrees of freedom. But this is at the expense of a deterioration of the conditioning of the algebraic systems. In some cases, the poor conditioning of the methods can rule out the use of iterative solvers.

The present paper aims at continuing the development of physics-based methods by formulating a general discontinuous Galerkin methods in the frequency domain using plane waves instead of polynomials to interpolate the solution. Throughout this paper the emphasize is on the central role played by the dispersion relation of the continuous problem in the definition of the numerical discretization. The method is presented for a general set of conservation equations. As an illustration it is applied to the linearized Euler equations in order to solve aeroacoustic propagation problems, that is the propagation of linear disturbances on a given steady flow.

In the context of aeroacoustic propagation, a large variety of computational methods have been studied, but two approaches have been mainly used. The first is to solve the linear potential theory where the mean flow and the acoustic perturbations are considered to be irrotational. This is generally done using standard finite element methods either in the frequency or time domain. This method is relatively inexpensive and it is possible to solve large-scale realistic problems. However, refraction of acoustic waves by rotational mean flows (such as the mixing layer of a jet) cannot be described and this effect can be crucial for some industrial applications (like noise radiation from turbofan exhausts). A more general approach is to use the linearized Euler equations which also describe vorticity and entropy waves in addition to acoustic waves. This model is generally solved in the time domain using high-order finite difference schemes (such as compact schemes

[25] or dispersion-relation-preserving schemes [26]). The use of discontinuous Galerkin methods has also become increasingly popular in the past few years. It should be noted that the use of physics-based numerical methods for aeroacoustic simulations has been rather limited, with the exception of the GFD and PUM for the linear potential theory [6,27–29].

The structure of this paper is as follows. Section 2 describes the formulation of the numerical method, including the variational formulation, the discretization of the solution and the trial function, the numerical flux and the boundary conditions. The similarities between the present numerical method and the UWVF are discussed in Section 2.6. Details of the implementation are given in Section 3. Section 4 discusses the accuracy and conditioning of the method by using a simple benchmark problem and compares these results with that of a high-order finite difference scheme. A modification of the variational formulation is introduced in Section 5 to deal more efficiently with point sources and the resulting singular solutions. Finally an example of an aeroacoustic propagation problem with a non-uniform flow is solved in Section 6.

2. Formulation of the method

We consider two-dimensional, linear, hyperbolic problems described by a general system of conservation equations written as follows:

$$\frac{\partial \mathbf{u}}{\partial t} + \frac{\partial}{\partial x}(\mathbf{A}\mathbf{u}) + \frac{\partial}{\partial y}(\mathbf{B}\mathbf{u}) = \mathbf{s}, \tag{1}$$

where $\mathbf{u}$ is the unknown vector representing the conserved quantities. The matrices $\mathbf{A}$ and $\mathbf{B}$ are square but not necessarily symmetric. These matrices can also be non-uniform, i.e., they may vary with position. The right-hand side $\mathbf{s}$ represents given external sources.

We consider time-harmonic problems with a $e^{-i\omega t}$ time dependence. The factor $e^{-i\omega t}$ is implied and omitted in what follows. The conservation equations can then be written:

$$-i\omega\mathbf{u} + \frac{\partial}{\partial x}(\mathbf{A}\mathbf{u}) + \frac{\partial}{\partial y}(\mathbf{B}\mathbf{u}) = \mathbf{s}. \tag{2}$$

Although the numerical methods will be described here in the general setting of the conservation Eq. (2), we are primarily interested in solving the linearized Euler equations (LEE) which represent the propagation of linear disturbances on a steady base flow. In the case of a homentropic flow (entropy is constant and uniform), only the conservation of mass and momentum are required and the LEE can be formulated as follows:

$$\mathbf{u} = \begin{bmatrix} \rho' \\ (\rho u)' \\ (\rho v)' \end{bmatrix}, \quad \mathbf{A} = \begin{bmatrix} 0 & 1 & 0 \\ c_0^2 - u_0^2 & 2u_0 & 0 \\ -u_0 v_0 & v_0 & u_0 \end{bmatrix}, \quad \mathbf{B} = \begin{bmatrix} 0 & 0 & 1 \\ -u_0 v_0 & v_0 & u_0 \\ c_0^2 - v_0^2 & 0 & 2v_0 \end{bmatrix}, \tag{3}$$

where ρ_0 denotes the mean density, $\mathbf{v}_0 = (u_0, v_0)^{\mathrm{T}}$ the velocity and c_0 the sound speed. The components of $\mathbf{u}$ represent respectively the linear perturbations of density ρ' and momentum $(\rho u)'$, $(\rho v)'$.

2.1. Variational formulation

We consider the variational formulation of the time-harmonic conservation Eq. (2) on a computational domain Ω which is decomposed into a set of non-overlapping finite elements $\{\Omega_e\}_{e=1,\ldots,N_e}$. The solution $\mathbf{u}$ is allowed to be discontinuous across the element boundaries. The variational statement is therefore written as a sum over the finite elements:

$$\sum_e \int_{\Omega_e} -i\omega\mathbf{v}^{\mathrm{T}}\mathbf{u} + \mathbf{v}^{\mathrm{T}}\frac{\partial}{\partial x}(\mathbf{A}\mathbf{u}) + \mathbf{v}^{\mathrm{T}}\frac{\partial}{\partial y}(\mathbf{B}\mathbf{u})\mathrm{d}\Omega = \sum_e \int_{\Omega_e} \mathbf{v}^{\mathrm{T}}\mathbf{s}\mathrm{d}\Omega, \quad \forall \mathbf{v},$$

where $^{\mathrm{T}}$ denotes the Hermitian transpose (transpose and complex conjugate) and $\mathbf{v}$ is the trial function associated to the unknown vector $\mathbf{u}$. Derivatives can then be integrated by parts:

$$\sum_e \int_{\Omega_e} -\mathrm{i}\omega \mathbf{v}^{\mathrm{T}}\mathbf{u} - \frac{\partial \mathbf{v}^{\mathrm{T}}}{\partial x}\mathbf{A}\mathbf{u} - \frac{\partial \mathbf{v}^{\mathrm{T}}}{\partial y}\mathbf{B}\mathbf{u}\mathrm{d}\Omega + \sum_e \int_{\partial\Omega_e} \mathbf{v}^{\mathrm{T}}\mathbf{A}\mathbf{u}n_x + \mathbf{v}^{\mathrm{T}}\mathbf{B}\mathbf{u}n_y \mathrm{d}\Gamma = \sum_e \int_{\Omega_e} \mathbf{v}^{\mathrm{T}}\mathbf{s}\mathrm{d}\Omega, \quad \forall \mathbf{v}, \tag{4}$$

where $\partial\Omega_e$ is the contour of the element Ω_e with an outward unit normal $\mathbf{n} = (n_x, n_y)^{\mathrm{T}}$. An internal edge $\Gamma_{e,e'}$ of the finite element mesh is the interface between the elements Ω_e and $\Omega_{e'}$ together with a unit normal pointing outside Ω_e, see Fig. 1. One can write:

$$\sum_e \int_{\Omega_e} -\mathrm{i}\omega \mathbf{v}^{\mathrm{T}}\mathbf{u} - \frac{\partial \mathbf{v}^{\mathrm{T}}}{\partial x}\mathbf{A}\mathbf{u} - \frac{\partial \mathbf{v}^{\mathrm{T}}}{\partial y}\mathbf{B}\mathbf{u}\mathrm{d}\Omega + \int_{\partial\Omega} \mathbf{v}^{\mathrm{T}}\mathbf{F}\mathbf{u}\mathrm{d}\Gamma + \sum_e \sum_{e'<e} \int_{\Gamma_{e,e'}} \left(\mathbf{v}^{\mathrm{T}}\mathbf{F}\mathbf{u}\right)_e + \left(\mathbf{v}^{\mathrm{T}}\mathbf{F}\mathbf{u}\right)_{e'} \mathrm{d}\Gamma = \sum_e \int_{\Omega_e} \mathbf{v}^{\mathrm{T}}\mathbf{s}\mathrm{d}\Omega, \quad \forall \mathbf{v}. \tag{5}$$

In the second integral, $\partial\Omega$ is the external boundary of the computational domain. In the integral over the edges $\Gamma_{e,e'}$, the subscripts $(\cdot)_e$ and $(\cdot)_{e'}$ indicate on which side of the edge the term is evaluated.

We have also introduced the flux matrix $\mathbf{F} = \mathbf{A}n_x + \mathbf{B}n_y$. The vector $\mathbf{Fu}$ represents the normal flux of the conserved quantities through the edge $\Gamma_{e,e'}$. In (5), the flux is computed independently on both sides of the edges. For the solution to satisfy the conservation Eq. (2), the normal flux should be conserved across each edge, that is,

$$\mathbf{F}_e\mathbf{u}_e = -\mathbf{F}_{e'}\mathbf{u}_{e'} = \mathbf{f}_{e,e'}(\mathbf{u}_e, \mathbf{u}_{e'}), \quad \text{on } \Gamma_{e,e'}.$$

where $\mathbf{f}_{e,e'}$ is a numerical flux which can be defined as a linear function of the solutions $\mathbf{u}_e$ and $\mathbf{u}_{e'}$ on both sides of the edges. The integral over the internal edges is modified as follows:

$$\sum_e \sum_{e'<e} \int_{\Gamma_{e,e'}} \left(\mathbf{v}^{\mathrm{T}}\mathbf{F}\mathbf{u}\right)_e + \left(\mathbf{v}^{\mathrm{T}}\mathbf{F}\mathbf{u}\right)_{e'} \mathrm{d}\Gamma = \sum_e \sum_{e'<e} \int_{\Gamma_{e,e'}} (\mathbf{v}_e - \mathbf{v}_{e'})^{\mathrm{T}}\mathbf{f}_{e,e'}(\mathbf{u}_e, \mathbf{u}_{e'})\mathrm{d}\Gamma.$$

The numerical flux used here will be described later on in Section 2.4.

2.2. The dispersion analysis and the plane wave basis

The key aspect of the present numerical method is to approximate the solution in each element as a sum of plane waves. For this approximation to be efficient the plane waves are taken to be local solutions of the problem at hand. In the numerical model, the coefficients of the continuous equations are approximated by piecewise constant functions. That is the matrices $\mathbf{A}$ and $\mathbf{B}$ are considered constant in each element. Therefore, the plane wave basis for each element is found by solving the homogeneous conservation Eq. (2) with constant coefficients:

$$-\mathrm{i}\omega\mathbf{u} + \mathbf{A}\frac{\partial \mathbf{u}}{\partial x} + \mathbf{B}\frac{\partial \mathbf{u}}{\partial y} = 0. \tag{6}$$

To define the finite element basis, we seek plane wave solutions of (6) with amplitude $\mathbf{r}$, direction θ and wavenumber k:

$$\mathbf{u} = \mathbf{r}\exp(\mathrm{i}kx\cos\theta + \mathrm{i}ky\sin\theta). \tag{7}$$

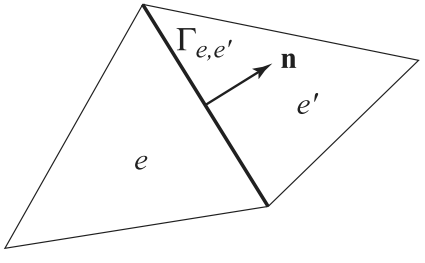

Fig. 1. An edge $\Gamma_{e,e'}$ between the elements Ω_e and $\Omega_{e'}$.

It is crucial to note that finding solutions of (6) and (7) is equivalent to a dispersion analysis of the equations at hand. Upon introducing the plane wave solution in Eq. (6), one obtains the following eigenvalue problem:

$$\mathbf{E}\mathbf{r} = \lambda\mathbf{r}, \quad \text{with } \mathbf{E} = \mathbf{A}\cos\theta + \mathbf{B}\sin\theta \quad \text{and } \lambda = \frac{\omega}{k}, \tag{8}$$

where the eigenvalue λ is the phase speed of the plane wave and the amplitude vector $\mathbf{r}$ is the right eigenvector of the matrix $\mathbf{E}$. The corresponding characteristic equation is simply:

$$\det(\mathbf{E} - \lambda\mathbf{I}) = 0 \quad \Longleftrightarrow \quad \det(k\cos\theta\mathbf{A} + k\sin\theta\mathbf{B} - \omega\mathbf{I}) = 0,$$

where $\mathbf{I}$ denotes the identity matrix. For a given wave direction θ one can obtain a set of eigenvalues λ_n associated to eigenvectors $\mathbf{r}_n$. The properties of time-dependent problems of the form (1) are preferably described in terms of their characteristics. For time-harmonic problems, the dispersion relation embodies the same information since each pair $(\lambda_n, \mathbf{r}_n)$ corresponds to a characteristic of the time-dependent partial differential equations.

When applied to the linearized Euler Eqs. (2) and (3) the dispersion analysis yields the following eigenvalues:

$$\lambda_1 = \mathbf{v}_0 \cdot \boldsymbol{\theta}, \quad \lambda_2 = \mathbf{v}_0 \cdot \boldsymbol{\theta} - c_0, \quad \lambda_3 = \mathbf{v}_0 \cdot \boldsymbol{\theta} + c_0, \tag{9}$$

where $\boldsymbol{\theta} = (\cos\theta, \sin\theta)^{\mathrm{T}}$ is the unit vector with direction θ. The corresponding wavenumbers are

$$k_1 = \frac{\omega}{\mathbf{v}_0 \cdot \boldsymbol{\theta}}, \quad k_2 = \frac{\omega}{\mathbf{v}_0 \cdot \boldsymbol{\theta} - c_0}, \quad k_3 = \frac{\omega}{\mathbf{v}_0 \cdot \boldsymbol{\theta} + c_0}. \tag{10}$$

And the corresponding eigenvectors are:

$$\mathbf{r}_1 = \begin{bmatrix} 0 \\ -c_0\sin\theta \\ c_0\cos\theta \end{bmatrix}, \quad \mathbf{r}_2 = \begin{bmatrix} 1 \\ u_0 - c_0\cos\theta \\ v_0 - c_0\sin\theta \end{bmatrix}, \quad \mathbf{r}_3 = \begin{bmatrix} 1 \\ u_0 + c_0\cos\theta \\ v_0 + c_0\sin\theta \end{bmatrix}. \tag{11}$$

The first eigenvector corresponds to vorticity waves which produce a rotational velocity field but no perturbation of pressure. These vorticity waves are simply convected with the mean flow. The two other eigenvectors correspond to acoustic waves which produce a potential velocity field, the two acoustic waves propagating in opposite directions. It should be emphasized that the acoustic and vortical waves are fundamentally different as the former are propagating in every direction while the latter is transported by the mean flow.

In the case of a non-uniform mean flow vorticity and acoustic perturbations are fully coupled. It is not possible to derive a systematic distinction between the two types of waves. It is also not possible to carry out a dispersion analysis. However, if one assumes a continuous mean flow, one can define around any point a sufficiently small neighborhood where it is possible to approximate the mean flow as locally uniform (this is essentially the assumption made by using piecewise constant matrices $\mathbf{A}$ and $\mathbf{B}$). Therefore at any point the hydrodynamic and acoustic fields can be represented *locally* as a sum of plane waves propagating in various directions.

The eigenvalues k_n and eigenvectors $\mathbf{r}_\mathrm{n}$ of the dispersion analysis (8) form a continuous family of solutions for the parameter θ. This means that any solution of Eq. (6) can be described as an infinite sum of plane waves where all the directions $\theta \in [0, 2\pi]$ contribute to represent the solution. However, for the purpose of devising a numerical scheme (which is inevitably finite dimensional), one has to select a *finite* number of planes waves.

As a consequence, the solution is approximated locally in each element by a finite set of plane waves representing the acoustic and vorticity perturbations:

$$\mathbf{u}(\mathbf{x}) = \sum_{n=1}^{N_w^e} a_n^e \mathbf{U}_n^e \exp(\mathrm{i}k_n^e \boldsymbol{\theta}_n^e \cdot \mathbf{x}), \quad \text{on } \Omega_e. \tag{12}$$

The superscript e indicates that the parameters of the finite element basis can be chosen independently in each element. This is obviously the case when the coefficient matrices **A** and **B** are non-uniform since in this case the plane waves obtained with the dispersion analysis will differ from one element to the next. But some other parameters, independent of the mean flow, can also be adjusted in each element, such as the number and directions of plane waves.

The degrees of freedom of the finite element basis (12) are the wave amplitudes a_n^e. We use N_a^e plane waves for the acoustic part of the solution and N_h^e waves for the hydrodynamic part. The total number of waves used for the element e is $N_w^e = N_a^e + N_h^e$.

Following the results of the dispersion analysis for the LEE, the wavenumber k_n^e and amplitudes $\mathbf{U}_n^e$ of the acoustic plane waves are defined by

$$k_n^e = \frac{\omega}{\mathbf{v}_0^e \cdot \boldsymbol{\theta}_n^e + c_0^e}, \quad \mathbf{U}_n^e = \begin{bmatrix} 1 \\ u_0^e + c_0^e \cos\theta_n^e \\ v_0^e + c_0^e \sin\theta_n^e \end{bmatrix}, \quad \text{with } 1 \leqslant n \leqslant N_a^e. \tag{13}$$

In a subsonic flow, the acoustic waves can propagate in any direction. Therefore, the N_a^e acoustic plane waves are evenly spaced in the interval $[0, 2\pi]$ as depicted in Fig. 2. The direction θ_n^e are given by

$$\theta_n^e = (n-1)\Delta\theta, \quad \text{with } \Delta\theta = \frac{2\pi}{N_a^e}, \quad \text{with } 1 \leqslant n \leqslant N_a^e. \tag{14}$$

The angular interval between two plane waves is $\Delta\theta = 2\pi/N_a^e$. It is possible to consider more elaborate ways to define the acoustic wave directions, for instance by taking the mean flow direction into account [28,29].

The wavenumbers k_n^e and amplitudes $\mathbf{U}_n^e$ for the vorticity waves are

$$k_n^e = \frac{\omega}{\mathbf{v}_0^e \cdot \boldsymbol{\theta}_n^e}, \quad \mathbf{U}_n^e = \begin{bmatrix} 0 \\ -c_0^e \sin\theta_n^e \\ c_0^e \cos\theta_n^e \end{bmatrix}, \quad \text{with } N_a^e + 1 \leqslant n \leqslant N_w^e. \tag{15}$$

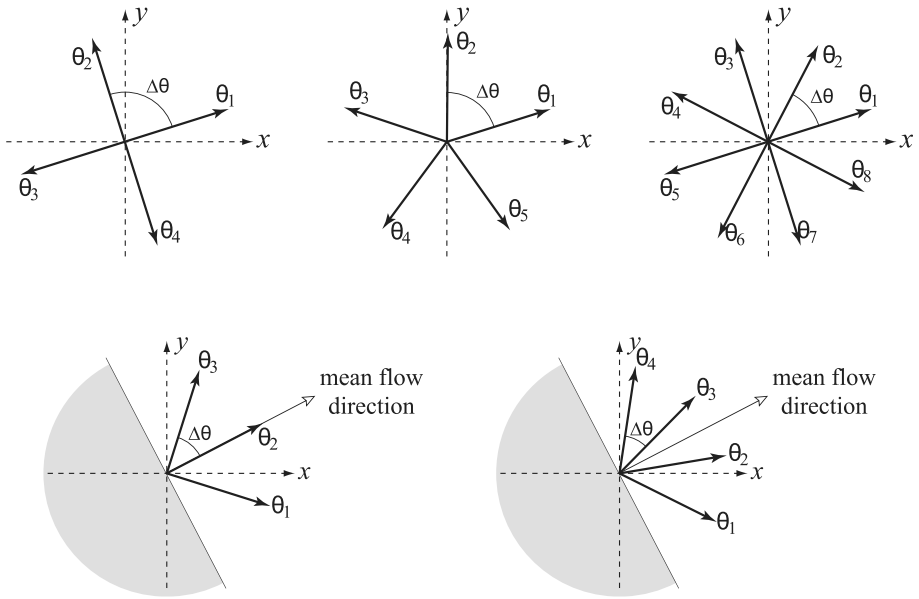

Fig. 2. Directions of the plane waves. Top: acoustic waves with 4, 5 and 8 directions. Bottom: vorticity waves with 3 and 4 directions, the shaded area represents the upstream direction where no vorticity wave can exist.

The vortical disturbances are convected downstream by the mean flow. So there is no vorticity wave propagating upstream of the mean flow, see Fig. 2. There is also no vorticity wave in the direction perpendicular to the mean flow since in this case $\mathbf{v}_0 \cdot \boldsymbol{\theta} = 0$ and the wavenumber goes to infinity. Therefore the directions of the hydrodynamic plane waves are evenly distributed on the interval $\theta_0 + (-\pi/2; \pi/2)$ where θ_0 is the direction of the mean flow, see Fig. 2. This corresponds to

$$\theta_n^e = \theta_0 - \pi/2 + (n - N_a^e)\Delta\theta, \quad \text{with } \Delta\theta = \frac{\pi}{1 + N_h^e}, \quad \text{with } N_a^e + 1 \leqslant n \leqslant N_w^e. \tag{16}$$

Dispersion properties are central in describing wave propagation phenomena. The plane wave solutions of the dispersion analysis are therefore particularly well-suited to build local approximations of the solutions since they capture the physics of the problem and allow for the dispersion relation to be built into the numerical approximations. It is worth noting two major differences between the plane wave discretization (12) and standard polynomial approximations. First, the linear relations between the various unknowns are accounted for in an exact manner (e.g. density and momentum for the linearized Euler equations). This is in contrast with standard computational schemes where the unknowns are discretized independently. Secondly, the different types of waves (acoustic and hydrodynamic) are described separately whereas standard methods discretize the total solutions induced by all the waves.

2.3. The trial functions and the adjoint problem

We now turn to the discretization of the trial function $\mathbf{v}$. An obvious and straightforward choice would be to use the same plane wave basis (12) as for the solution itself. It proves however more interesting to use the adjoint of Eq. (6) that was used to define the plane wave basis for $\mathbf{u}$. It is straightforward to show that the adjoint problem written for $\mathbf{v}$ is

$$\mathrm{i}\omega\mathbf{v} - \mathbf{A}^{\mathrm{T}}\frac{\partial \mathbf{v}}{\partial x} - \mathbf{B}^{\mathrm{T}}\frac{\partial \mathbf{v}}{\partial y} = 0. \tag{17}$$

The plane waves used to represent the trial function $\mathbf{v}$ are taken to be solutions of the adjoint problem. So we perform a second dispersion analysis by seeking plane wave solutions with amplitude $\mathbf{l}$, direction θ and wavenumber k:

$$\mathbf{v} = \mathbf{l}\exp(\mathrm{i}kx\cos\theta + \mathrm{i}ky\sin\theta).$$

This yields the following adjoint eigenvalue problem:

$$\mathbf{E}^{\mathrm{T}}\mathbf{l} = \lambda\mathbf{l}, \quad \text{with } \mathbf{E} = \mathbf{A}\cos\theta + \mathbf{B}\sin\theta, \text{ and } \lambda = \frac{\omega}{k}.$$

Thus $\mathbf{l}^{\mathrm{T}}$ corresponds to left eigenvectors of the matrix $\mathbf{E}$ with eigenvalue λ. It is interesting to note that the plane waves used for $\mathbf{u}$ and $\mathbf{v}$ are the right and left eigenvectors of the same matrix $\mathbf{E}$. The right and left eigenvectors share the same eigenvalues λ and satisfy the bi-orthogonality property, that is $\mathbf{r}_n$ and $\mathbf{l}_m$ are orthogonal if $\lambda_m \neq \lambda_n$. As for the unknown vector $\mathbf{u}$, the trial function $\mathbf{v}$ is approximated locally by a finite sum of plane waves:

$$\mathbf{v}(\mathbf{x}) = \sum_{m=1}^{N_w^e} b_m^e \mathbf{V}_m^e \exp(\mathrm{i}k_m^e \boldsymbol{\theta}_m^e \cdot \mathbf{x}), \quad \text{on } \Omega_e. \tag{18}$$

The degrees of freedom for $\mathbf{v}$ are the wave amplitudes b_m^e.

For the linearized Euler equations, the eigenvectors of the adjoint problem are:

$$\mathbf{l}_1 = \begin{bmatrix} u_0\sin\theta - v_0\cos\theta \\ -\sin\theta \\ \cos\theta \end{bmatrix}, \quad \mathbf{l}_2 = \begin{bmatrix} -c_0 - \mathbf{v}_0\cdot\boldsymbol{\theta} \\ \cos\theta \\ \sin\theta \end{bmatrix}, \quad \mathbf{l}_3 = \begin{bmatrix} c_0 - \mathbf{v}_0\cdot\boldsymbol{\theta} \\ \cos\theta \\ \sin\theta \end{bmatrix},$$

and the eigenvalues are identical to that of the direct problem given in (9). The numbers of acoustic and vorticity waves N_a^e and N_h^e used in (18) are the same as for the plane wave basis of $\mathbf{u}$. Although it is possible to use

different set of wave directions for $\mathbf{u}$ and $\mathbf{v}$, here the wave directions θ_m^e are also given by (14) and (16). Therefore, for acoustic waves we use:

$$k_m^e = \frac{\omega}{\mathbf{v}_0^e \cdot \boldsymbol{\theta}_m^e + c_0^e}, \quad \mathbf{V}_m^e = \begin{bmatrix} c_0^e - \mathbf{v}_0^e \cdot \boldsymbol{\theta}_m^e \\ \cos\theta_m^e \\ \sin\theta_m^e \end{bmatrix}, \quad \text{with } 1 \leqslant m \leqslant N_a.$$

And for the vorticity waves:

$$k_m^e = \frac{\omega}{\mathbf{v}_0^e \cdot \boldsymbol{\theta}_m^e}, \quad \mathbf{V}_m^e = \begin{bmatrix} u_0^e \sin\theta_m^e - v_0^e \cos\theta_m^e \\ -\sin\theta_m^e \\ \cos\theta_m^e \end{bmatrix}, \quad \text{with } N_a + 1 \leqslant m \leqslant N_w.$$

The benefit of using the adjoint problem is a significant simplification of the variational formulation (5). The first term in the variational formulation can be rewritten as follows:

$$\int_{\Omega_e} -\mathrm{i}\omega \mathbf{v}^{\mathrm{T}}\mathbf{u} - \frac{\partial \mathbf{v}^{\mathrm{T}}}{\partial x}\mathbf{A}\mathbf{u} - \frac{\partial \mathbf{v}^{\mathrm{T}}}{\partial y}\mathbf{B}\mathbf{u}\mathrm{d}\Omega = \int_{\Omega_e} \left(\mathrm{i}\omega\mathbf{v} - \mathbf{A}^{\mathrm{T}}\frac{\partial \mathbf{v}}{\partial y} - \mathbf{B}^{\mathrm{T}}\frac{\partial \mathbf{v}}{\partial y}\right)^{\mathrm{T}} \mathbf{u}\mathrm{d}\Omega.$$

The term in brackets is precisely the adjoint equation. Hence when $\mathbf{v}$ is solution of the adjoint problem the integral over the elements Ω_e vanishes. This represents a significant reduction of the computational complexity of the method.

If one was to use (12) to describe both $\mathbf{u}$ and $\mathbf{v}$, the scalar product $\mathbf{v}^{\mathrm{T}}\mathbf{u}$ would not be consistent in terms of physical units (in the case of the linearized Euler Eqs. (2) and (3), $\mathbf{u}$ and $\mathbf{v}$ would have components which are either mass density or momentum density, thus $\mathbf{v}^{\mathrm{T}}\mathbf{u}$ implies the sum of terms with different units). It can be easily seen that another consequence of using the adjoint problem to define the plane wave basis for $\mathbf{v}$ is that the variational formulation is now consistent in terms of physical units.

2.4. The numerical flux

The choice of a numerical flux is crucial to devise efficient discontinuous Galerkin methods. A large variety of numerical fluxes have been proposed for various problems (advection, diffusion, etc), see for instance [30,31]. In the present method, an upwind flux-vector splitting method is used, firstly because it is a simple and well-known technique but more importantly because it is closely related with the dispersion analysis that yields the plane wave basis.

Consider an edge $\Gamma_{e,e'}$ between the elements e and e'. The flux matrices $\mathbf{F}$ defined on both sides of the edge can be written in terms of their eigenvalues and eigenvectors:

$$\mathbf{F} = \mathbf{W}\boldsymbol{\Lambda}\mathbf{W}^{-1}, \tag{19}$$

where $\boldsymbol{\Lambda}$ is the diagonal matrix with the eigenvalues λ_n and $\mathbf{W}$ is the matrix of eigenvectors $\mathbf{w}_n$:

$$\boldsymbol{\Lambda} = \mathrm{diag}(\lambda_1, \lambda_2, \lambda_3, \ldots), \quad \mathbf{W} = [\mathbf{w}_1 \quad \mathbf{w}_2 \quad \mathbf{w}_3 \quad \ldots]. \tag{20}$$

The eigenvalues λ_n represent the phase velocity of each eigensolution in the direction normal to the edge. For a problem with non-uniform coefficients, the eigenvalues and eigenvectors are different on each side of the edge. The diagonal matrix $\boldsymbol{\Lambda}$ is split in two matrices: $\boldsymbol{\Lambda} = \boldsymbol{\Lambda}^+ + \boldsymbol{\Lambda}^-$ where $\boldsymbol{\Lambda}^+$ contains only the positive eigenvalues while $\boldsymbol{\Lambda}^-$ contains only the strictly negative eigenvalues:

$$\boldsymbol{\Lambda}^{\pm} = \mathrm{diag}(\lambda_1^{\pm}, \lambda_2^{\pm}, \lambda_3^{\pm}, \ldots), \quad \lambda_i^+ = \begin{cases} \lambda_i & \text{if } \lambda_i \geqslant 0 \\ 0 & \text{if } \lambda_i < 0 \end{cases}, \quad \lambda_i^- = \begin{cases} 0 & \text{if } \lambda_i \geqslant 0 \\ \lambda_i & \text{if } \lambda_i < 0 \end{cases}.$$

The numerical flux $\mathbf{f}(\mathbf{u}_e, \mathbf{u}_{e'})$ can then be decomposed into two terms using upwinding:

$$\mathbf{f}_{e,e'}(\mathbf{u}_e, \mathbf{u}_{e'}) = \mathbf{F}_{e,e'}^{+}\mathbf{u}_e + \mathbf{F}_{e,e'}^{-}\mathbf{u}_{e'}.$$

The first term represents the flux associated with the waves travelling from the element e to the element e'. Thus this term is computed using the solution from the element e. On the other hand, the second term represents the flux from e' to e and it is evaluated with the solution from the element e'. The split flux matrices are defined as follows:

$$\mathbf{F}^{+}_{e,e'} = \mathbf{W}_{e,e'}\boldsymbol{\Lambda}^{+}_{e}\mathbf{W}^{-1}_{e,e'}, \text{ and } \quad \mathbf{F}^{-}_{e,e'} = \mathbf{W}_{e,e'}\boldsymbol{\Lambda}^{-}_{e'}\mathbf{W}^{-1}_{e,e'}, \tag{21}$$

where $\mathbf{W}_{e,e'}$ is a matrix of eigenvectors where each column associated to a positive eigenvalue is the corresponding eigenvector from the element e while for negative eigenvalues the corresponding column in $\mathbf{W}_{e,e'}$ is the eigenvector calculated in the element e'. With uniform coefficients, the matrix $\mathbf{W}_{e,e'}$ reduces to $\mathbf{W}$. The variational formulation (5) of the method is now written

$$\sum_{e}\sum_{e'<e}\int_{\Gamma_{e,e'}}(\mathbf{v}_e-\mathbf{v}_{e'})^{\mathrm{T}}\left(\mathbf{F}^{+}_{e,e'}\mathbf{u}_e+\mathbf{F}^{-}_{e,e'}\mathbf{u}_{e'}\right)\mathrm{d}\Gamma+\int_{\partial\Omega}\mathbf{v}^{\mathrm{T}}\mathbf{F}\mathbf{u}\mathrm{d}\Gamma=\sum_{e}\int_{\Omega_e}\mathbf{v}^{\mathrm{T}}\mathbf{s}\mathrm{d}\Omega. \tag{22}$$

It is interesting to note that the flux-vector splitting method is closely related to the dispersion analysis (8) which yields the plane wave basis. In fact the flux-splitting method involves essentially a dispersion analysis of the equations in the direction normal to the edge. This is seen more clearly by writing the eigenvalue problem for the flux matrix $\mathbf{F}$ as follows:

$$\mathbf{F}\mathbf{w}=\lambda\mathbf{w}, \quad \text{with } \mathbf{F}=\mathbf{A}n_x+\mathbf{B}n_y.$$

It is then obvious that the latter expression is a particular case of the eigenvalue problem of the dispersion analysis (8) with the wave direction $\boldsymbol{\theta}$ corresponding to the normal $\mathbf{n}$. Therefore, it should be emphasized that, in the present numerical method, *the dispersion relation of the continuous problem forms the basis for the numerical approximation of the flux between elements and for the discretization of the solutions and the trial functions within the elements*.

In the case of the linearized Euler Eqs. (2) and (3) the eigenvalues of the flux matrix are the same as in Sections 2.2 and 2.3, except that the direction $\boldsymbol{\theta}$ is now replaced by $\mathbf{n}$:

$$\lambda_1=\mathbf{v}_0\cdot\mathbf{n}, \quad \lambda_2=\mathbf{v}_0\cdot\mathbf{n}-c_0, \quad \lambda_3=\mathbf{v}_0\cdot\mathbf{n}+c_0. \tag{23}$$

The corresponding eigenvectors are:

$$\mathbf{w}_1=\begin{bmatrix}0\\-c_0n_y\\c_0n_x\end{bmatrix}, \quad \mathbf{w}_2=\begin{bmatrix}1\\u_0-c_0n_x\\v_0-c_0n_y\end{bmatrix}, \quad \mathbf{w}_3=\begin{bmatrix}1\\u_0+c_0n_x\\v_0+c_0n_y\end{bmatrix}. \tag{24}$$

And we define the matrix of eigenvectors and its inverse:

$$\mathbf{W}=\begin{bmatrix}0&1&1\\-c_0n_y&u_0-c_0n_x&u_0+c_0n_x\\c_0n_x&v_0-c_0n_y&v_0+c_0n_y\end{bmatrix}, \quad \mathbf{W}^{-1}=\frac{1}{2c_0}\begin{bmatrix}2(u_0n_y-v_0n_x)&-2n_y&2n_x\\c_0+\mathbf{v}_0\cdot\mathbf{n}&-n_x&-n_y\\c_0-\mathbf{v}_0\cdot\mathbf{n}&n_x&n_y\end{bmatrix}. \tag{25}$$

For problems with non-uniform coefficients, the split flux matrices $\mathbf{F}^{\pm}_{e,e'}$ are built using Eqs. (21) together with (23) and (24).

2.5. Boundary conditions

Various conditions can be applied on the boundary of the computational domain and one has to modify accordingly the boundary integral on $\partial\Omega$ in (22). Two types of boundary conditions are considered here: vibrating walls and ghost cells which can be used to enforce a given solution.

2.5.1. Vibrating wall

On a vibrating wall, the mean flow is tangential to the boundary so we have $\mathbf{v}_0\cdot\mathbf{n}=0$. Furthermore the normal velocity at the wall is given by $\mathbf{v}\cdot\mathbf{n}=V$ on $\partial\Omega$. To implement this boundary condition, it is convenient

to use the flux-vector splitting by introducing the eigenvalues and eigenvectors of the flux matrix $\mathbf{F}$, see (19). The integrand in the boundary integral can be rewritten as follows:

$$\mathbf{v}^{\mathrm{T}}\mathbf{F}\mathbf{u} = \mathbf{v}^{\mathrm{T}}\mathbf{W}\boldsymbol{\Lambda}\mathbf{W}^{-1}\mathbf{u} = \mathbf{v}^{\mathrm{T}}\mathbf{W}\begin{bmatrix} \lambda_1\rho_0\mathbf{n}\times\mathbf{v} \\ \lambda_2(\rho' c_0 - \rho_0\mathbf{v}\cdot\mathbf{n})/(2c_0) \\ \lambda_3(\rho' c_0 + \rho_0\mathbf{v}\cdot\mathbf{n})/(2c_0) \end{bmatrix}. \tag{26}$$

Using Eq. (23) and the fact that $\mathbf{v}_0\cdot\mathbf{n} = 0$, we get $\lambda_1 = 0$, $\lambda_2 = -c_0$ and $\lambda_3 = c_0$. After some algebra, the integrand can be further simplified:

$$\mathbf{v}^{\mathrm{T}}\mathbf{F}\mathbf{u} = \mathbf{v}^{\mathrm{T}}\begin{bmatrix} 0 & 0 & 0 \\ c_0^2 n_x & 0 & 0 \\ c_0^2 n_y & 0 & 0 \end{bmatrix}\mathbf{u} + \mathbf{v}^{\mathrm{T}}\begin{bmatrix} \rho_0 V \\ \rho_0 u_0 V \\ \rho_0 v_0 V \end{bmatrix}.$$

The second term represents the forcing of the vibrating wall and contributes to the right-hand side in the variational formulation (22).

2.5.2. Ghost cell

Ghost cells can be used on the boundary when the solution outside the computational domain is known $\mathbf{u} = \mathbf{g}(\mathbf{x})$. The basic idea behind the ghost cell is to treat the boundary as an internal edge and to use the numerical flux to derive the forcing induced by the prescribed solution $\mathbf{g}$ outside the domain. An interesting property is that the amplitudes of the outgoing waves are not imposed and thus the ghost cells can also be used as a simple, first-order non-reflecting boundary condition. With the flux-vector splitting method, the integral over the internal edges is given in (22) and can be rewritten as follows for the boundary of the computational domain:

$$\int_{\partial\Omega} (\mathbf{v}_e - \mathbf{v}_{e'})^{\mathrm{T}}(\mathbf{F}^+\mathbf{u}_e + \mathbf{F}^-\mathbf{u}_{e'})\mathrm{d}\Gamma,$$

where $\mathbf{u}_e = \mathbf{u}$ represents the unknown solution inside the computational domain while $\mathbf{u}_{e'} = \mathbf{g}$ is the solution outside. The trial function $\mathbf{v}_{e'}$ is zero since $\mathbf{u}_{e'}$ is known and the boundary integral reads

$$\int_{\partial\Omega} \mathbf{v}^{\mathrm{T}}\mathbf{F}\mathbf{u}\mathrm{d}\Gamma = \int_{\partial\Omega} \mathbf{v}^{\mathrm{T}}\mathbf{F}^+\mathbf{u}\mathrm{d}\Gamma + \int_{\partial\Omega} \mathbf{v}^{\mathrm{T}}\mathbf{F}^-\mathbf{g}\mathrm{d}\Gamma. \tag{27}$$

The second term represent the forcing of the imposed solution $\mathbf{g}$ and contributes to the right-hand side in the variational formulation (22).

2.6. Similarity with the ultra weak variational formulation

The Ultra Weak Variational Formulation was originally devised by Després and Cessenat [14–17] and it has then been significantly developed by Huttunen et al. [18–20]. An advantage of the UWVF is that its implementation is fairly straightforward since the element matrix can be evaluated in closed form. This is in contrast with other methods such as the Partition of Unity Methods where special numerical integration schemes are required. Although the UWVF has emerged as a separate numerical method, it can be shown that it is in fact a particular category of discontinuous Galerkin methods with plane waves. This can be illustrated by showing that, with no flow, the present discontinuous Galerkin method for the linearized Euler equations reduces to the UWVF for Helmholtz equation as presented in [18]. With $u_0 = v_0 = 0$ and c_0 constant, the expressions for the plane wave basis (12) and (18) are simplified as there is no vorticity waves. Using the numerical flux, the first term in the variational formulation (22) reads

$$\sum_e \sum_{e'<e} \int_{\Gamma_{e,e'}} \left(\mathbf{v}_e^{\mathrm{T}}\mathbf{F}^+\mathbf{u}_e + \mathbf{v}_e^{\mathrm{T}}\mathbf{F}^-\mathbf{u}_{e'} - \mathbf{v}_{e'}^{\mathrm{T}}\mathbf{F}^+\mathbf{u}_e - \mathbf{v}_{e'}^{\mathrm{T}}\mathbf{F}^-\mathbf{u}_{e'}\right)\mathrm{d}\Gamma.$$

The components of $\mathbf{v}$ are denoted $\mathbf{v} = (q, \alpha, \beta)^{\mathrm{T}}$ so that q, α and β are the trial function corresponding to ρ', $(\rho u)'$ and $(\rho v)'$, respectively. Upon using expressions (20) and (25) one can derive

$$\mathbf{v}^{\mathrm{T}}\mathbf{F}^{+}\mathbf{u} = \frac{+1}{2}\overline{(q + c_0\alpha n_x + c_0\beta n_y)}(c_0\rho' + (\rho u)'n_x + (\rho v)'n_y),$$

$$\mathbf{v}^{\mathrm{T}}\mathbf{F}^{-}\mathbf{u} = \frac{-1}{2}\overline{(q - c_0\alpha n_x - c_0\beta n_y)}(c_0\rho' - (\rho u)'n_x - (\rho v)'n_y),$$

where the overbar denotes the complex conjugate. The following expressions can be deduced from the direct and adjoint problems (6), (17):

$$(\rho u)'n_x + (\rho v)'n_y = \frac{c_0^2}{\mathrm{i}\omega}\frac{\partial\rho}{\partial n}, \quad \alpha n_x + \beta n_y = \frac{1}{\mathrm{i}\omega}\frac{\partial q}{\partial n}.$$

Then one can derive

$$\mathbf{v}^{\mathrm{T}}\mathbf{F}^{+}\mathbf{u} = \frac{c_0^3}{2\omega^2}\overline{\left(\frac{\mathrm{i}\omega}{c_0}q + \frac{\partial q}{\partial n}\right)}\left(\frac{\mathrm{i}\omega}{c_0}\rho + \frac{\partial\rho}{\partial n}\right), \quad \mathbf{v}^{\mathrm{T}}\mathbf{F}^{-}\mathbf{u} = \frac{-c_0^3}{2\omega^2}\overline{\left(\frac{\mathrm{i}\omega}{c_0}q - \frac{\partial q}{\partial n}\right)}\left(\frac{\mathrm{i}\omega}{c_0}\rho - \frac{\partial\rho}{\partial n}\right). \tag{28}$$

And finally the first term in (22) becomes

$$\frac{c_0^3}{2\omega^2}\sum_e\sum_{e'<e}\int_{\Gamma_{e,e'}}\overline{\left(\frac{\mathrm{i}\omega}{c_0}q_e + \frac{\partial q_e}{\partial n}\right)}\left(\frac{\mathrm{i}\omega}{c_0}\rho_e + \frac{\partial\rho_e}{\partial n_e}\right) - \overline{\left(\frac{\mathrm{i}\omega}{c_0}q_e - \frac{\partial q_e}{\partial n}\right)}\left(\frac{\mathrm{i}\omega}{c_0}\rho_{e'} - \frac{\partial\rho_{e'}}{\partial n}\right)$$
$$- \overline{\left(\frac{\mathrm{i}\omega}{c_0}q_{e'} + \frac{\partial q_{e'}}{\partial n}\right)}\left(\frac{\mathrm{i}\omega}{c_0}\rho_e + \frac{\partial\rho_e}{\partial n_e}\right) + \overline{\left(\frac{\mathrm{i}\omega}{c_0}q_{e'} - \frac{\partial q_{e'}}{\partial n}\right)}\left(\frac{\mathrm{i}\omega}{c_0}\rho_{e'} - \frac{\partial\rho_{e'}}{\partial n}\right)\mathrm{d}\Gamma.$$

This is equivalent to the Ultra Weak Variational Formulation given by Eq. (10) in Ref. [18] for the Helmholtz equation. The similarity between discontinuous Galerkin methods and ultra weak variational formulation was also observed independently by Monk and Huttunen in the context of electromagnetism [21].

Therefore, the present discontinuous Galerkin method with plane waves can also be viewed as an extension of the UWVF to the linearized Euler equations. The fact that UWVF methods can be formulated as discontinuous Galerkin methods is quite useful as it allows to build upon the vast literature available on DGM rather than developing independently the UWVF. In particular, the UWVF requires the formulation of continuity conditions to be weakly imposed at the interfaces between elements. These *ad hoc* conditions are devised independently for each problem by inspection of the equations at hand. In the context of DGM, the use of a numerical flux provides a general framework to derive these continuity conditions for any system of conservation equations.

3. Implementation

To implement the numerical method, one has to evaluate the integrals in the variational formulation (5). Inside each element the matrices **A** and **B** are approximated as constant and the plane wave basis (12) and (18) for the solution and the trial function involve only simple exponential functions. Therefore the integrands are exponentials. Thanks to the use of the adjoint problem for the trial functions the domain integral vanishes and one is left with integrals of exponentials along the edges of the mesh. For any polyhedral mesh, these edges are straight segments and it is straightforward to evaluate these integrals in closed form. This simplicity in the implementation of the method is an advantage compared to standard polynomial-based discontinuous Galerkin methods which require numerical Gauss integration schemes (except for standard finite volume methods which use constant interpolation), or other physics-based numerical methods (such as the Partition of Unity Method which requires special integration schemes [32,33]).

4. Benchmark problem

To study the properties of the proposed numerical method, we consider the problem of a single plane wave propagating in a uniform medium, see Fig. 3. This is very similar to performing a dispersion analysis of the numerical model and the simplistic nature of this benchmark problem allows for a detailed analysis of the properties of the numerical scheme (accuracy, conditioning and anisotropy). This benchmark problem has

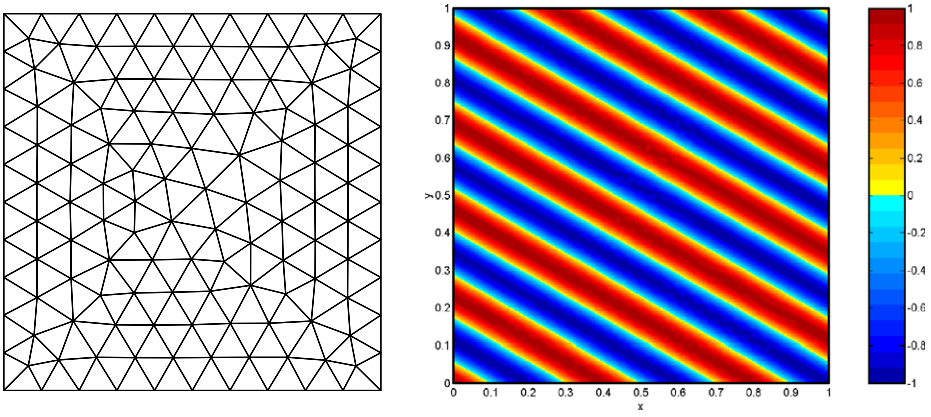

Fig. 3. Left: Finite element mesh of the computational domain (228 triangles); Right: Example of solution for an acoustic wave.

previously been used for several other numerical methods, for instance partition of unity methods [7,8] or discontinuous Galerkin methods with Lagrange multipliers [34,12].

The parameter of the problem are made non-dimensional, so we have $c_0 = 1$ and $\rho_0 = 1$. The mean flow is uniform with direction $\alpha = 0$ and Mach number $M = v_0/c_0 = 0.5$. The computational domain Ω is a 1×1 square meshed with unstructured triangular elements, see Fig. 3. Ghost cells are used on the boundary of the computational domain in order to generate a single plane wave. This wave can be either an acoustic or hydrodynamic disturbance and is obtained by defining $\mathbf{g}$ in Eq. (27) as

$$\mathbf{g} = \mathbf{G}\exp(\mathrm{i}k\boldsymbol{\theta}\cdot\mathbf{x}),$$

where θ is the direction of the plane wave and $\mathbf{G}$ and k are given by (13) for an acoustic wave and by (15) for a vorticity wave.

To assess the accuracy of the computational scheme the numerical error E is defined as the L^2 relative error on the unknown vector $\mathbf{u}$. That is

$$E = \frac{\|\mathbf{u} - \mathbf{u}_{ex}\|_{L_2(\Omega)}}{\|\mathbf{u}_{ex}\|_{L_2(\Omega)}},$$

where the exact solution is $\mathbf{u}_{ex} = \mathbf{g}$. Since both the numerical solutions and the exact solution are made of plane waves, this error can be evaluated in closed form using the integration technique described in [15, section III.D].

4.1. Anisotropy

First consider the anisotropy of the model, that is the influence of the wave direction on the numerical error. For acoustic waves, Fig. 4 shows the relative error plotted against the wave direction θ for different number of acoustic waves N_a in the plane wave basis (and with no vorticity wave, $N_h = 0$). The frequency is fixed $\omega = 20$ and the element size is $h = 0.1$. The relative error tends to increase when the wave propagates against the flow and this is due to the Doppler effect introduced by the mean flow. The acoustic wavelength is $2\pi/k$ with k given by (13) and it can be seen that acoustic waves are shorter or longer in the upstream or downstream directions, respectively.

To show more clearly the effect of the plane wave basis a second set of results is presented in Fig. 4 where the frequency is adjusted as the direction θ is varied so as to remove the Doppler effect introduced by the mean flow. In that way, the wavelength of the incident wave is independent of its direction and the number of elements per wavelength is held constant (we use 3 elements per wavelength in the present results). The error observed is now solely a function of the angular distance between the direction of the incident wave and the directions of the plane wave basis. The relative error decreases significantly when the wave direction is close to one of the directions of the plane waves basis (in fact the error drops to zero as there is strictly no

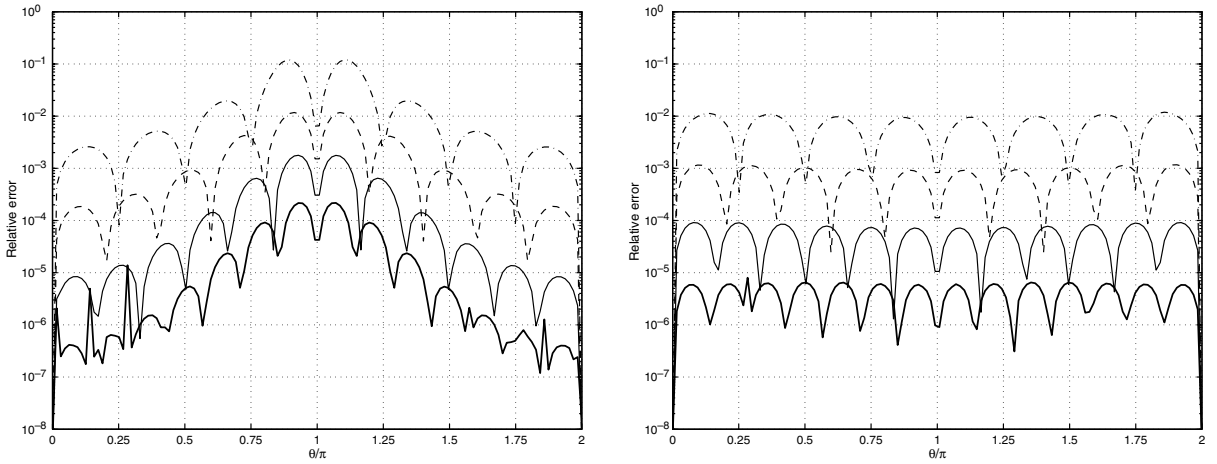

Fig. 4. Relative error versus the direction of the incident acoustic wave with $N_h = 0$ and $N_a = 8$ (dot–dashed line), $N_a = 10$ (dashed line), $N_a = 12$ (thin solid line) and $N_a = 14$ (thick solid line). Left: the frequency is constant; Right: the wavelength is constant.

error when the θ equals one of the directions of the plane wave basis). For instance, with 8 plane waves the error is constantly below 1% with 3 elements per wavelength. Furthermore, increasing the number of plane waves in the basis results in a significant reduction of the numerical error. For numerical methods based on plane waves, it is well known that increasing the number of plane waves is much more efficient than improving the mesh resolution (see Section 4.2).

The anisotropy for an incident vorticity wave is shown in Fig. 5 with $\omega = 10$ for different numbers of vorticity plane waves in the basis. The relative error becomes quite large when the incident vorticity wave is almost orthogonal to the mean flow (that is for $\theta = \pi/2$ and $\theta = 3\pi/2$). This is explained by noting that the wavelength of the vorticity waves is $2\pi/k$ with k given by (15). As the wave direction becomes orthogonal to the mean flow, the wavelength tends to zero and the number of elements per wavelength is tending to zero as well. The large error observed for $\theta = \pi/2$ and $\theta = 3\pi/2$ is therefore not a defect of the present numerical method but is due to the physics of the problem which render impossible the accurate resolution of vorticity waves nearly orthogonal to the mean flow. In fact, this problem can be reproduced with other numerical schemes for the linearized Euler equations (see for instance Fig. 11). As with acoustic waves, the numerical error for the vorticity waves decreases notably when the incident waves direction is close to one of the waves of the basis. Again increasing the number of plane waves yields a significant reduction of the relative error.

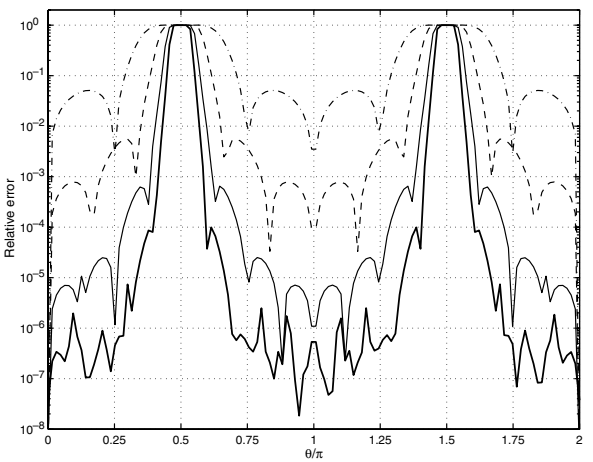

Fig. 5. Relative error versus the direction of the incident vorticity wave with $N_a = 0$ and $N_h = 3$ (dot–dashed line), $N_h = 5$ (dashed line), $N_h = 7$ (thin solid line) and $N_h = 9$ (thick solid line).

Although the large errors observed for $\theta = \pi/2$ and $\theta = 3\pi/2$ seems severe, in practice this is not important because a large part of the vorticity is convected with the flow and the amount of vorticity propagating at large angle is comparatively insignificant. For instance in turbulence modelling, the flow field is mainly composed of vortical disturbances and can be decomposed as a sum of plane waves using Fourier analysis. The velocity spectrum, which describes the amount of energy contained by the waves in each direction, decreases quickly for waves which are not parallel to the mean flow [35] (the energy of the waves perpendicular to the flow are indeed zero). This well-known behaviour of turbulent flows is embodied in the energy spectrums formulated by von Kármán and Liepmann.

For both acoustic and vortical waves, the results with very low level of errors are partly altered by the presence of peaks. These are induced by the poor conditioning of the numerical model for very accurate solutions. The issue of conditioning will be discussed in Section 4.3.

4.2. Convergence

We now consider the convergence of the model by plotting the accuracy against the mesh resolution which is generally given by the number of points per wavelength. With standard finite element methods, the degrees of freedom are generally the nodal values of the solutions and the number of degrees of freedom is directly proportional to the number of nodes of the mesh. With discontinuous Galerkin methods, the situation is more complicated since the degrees of freedom do not correspond to nodal values. It is therefore more convenient to define a number of degrees of freedom per wavelength which better represents the 'density' of information required to describe one wavelength λ. For a $L \times L$ square computational domain, this is done by considering a regular grid with n_{dof} nodes. The node spacing on such a grid is given by $L/(\sqrt{n_{\mathrm{dof}}} - 1)$ and the corresponding number of degrees of freedom per wavelength is $\lambda(\sqrt{n_{\mathrm{dof}}} - 1)/L$.

As shown in the previous section the accuracy is significantly influenced by the direction of the wave with respect to the flow and the plane wave basis. However, for realistic problems, the solution at any point in the computational domain is likely to be composed of waves propagating in different directions and it is therefore unrealistic to define the accuracy of the model in terms of one particular wave direction. From a practical point of view, one should rather consider the worst case by choosing the incident wave direction which results in the largest relative error. So we choose $\theta = 7\pi/8$ for the incident acoustic wave and $\theta = 4\pi/11$ for the vorticity wave. This yields conservative yet reliable estimates of the accuracy of the method for realistic problems.

Fig. 6 shows the convergence for an acoustic incident wave with different numbers of plane waves. Increasing the number of plane waves results in a significant increase of the rate of convergence. This is a well-known

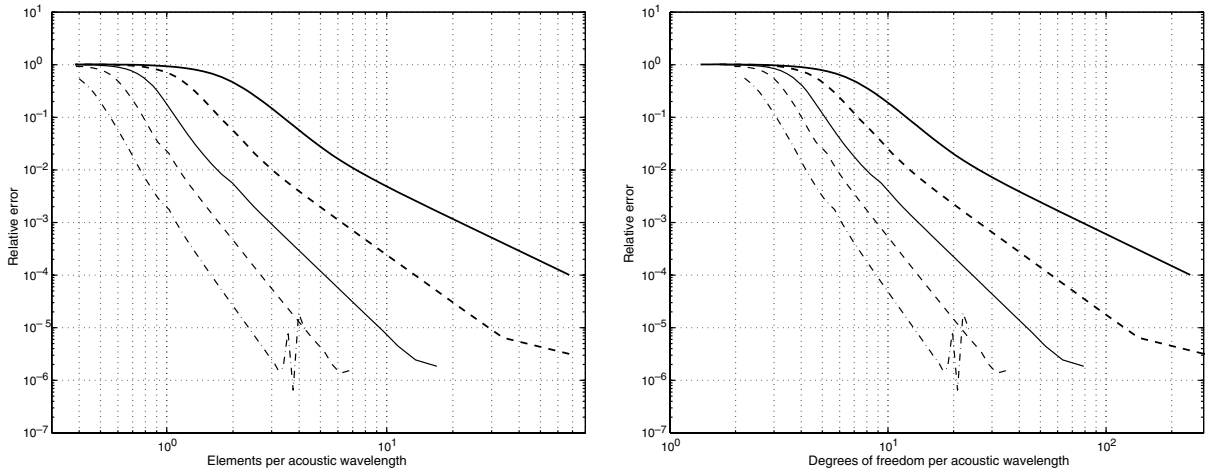

Fig. 6. Convergence for an incident acoustic waves with different number of acoustic plane waves in the basis. Relative error plotted against the number of elements per acoustic wavelength (left) and against the number of degrees of freedom per acoustic wavelength (right). $N_a = 6$ (thick solid line), $N_a = 8$ (thick dashed line), $N_a = 10$ (thin solid line), $N_a = 12$ (thin dashed line), $N_a = 14$ (thin dot–dashed line).

property of numerical methods using plane waves (and more generally of spectral methods) that increasing the number of basis functions is much more efficient than increasing the mesh resolution (in other words using p-refinement is more efficient than h-refinement). For more information on this general aspect of spectral methods see [7,8,36]. The rate of convergence with the number of plane waves is exponential while refining the mesh yields only an algebraic convergence. By analyzing the convergence results for various number of plane waves it is possible to infer that the rate of convergence of the numerical solution is the integer part of $(N_a - 1)/2$. As an illustration of the accuracy of the method, it is noted that with 14 plane waves the relative error falls below 1% with less than 5 degrees of freedom per wavelength or less than 0.8 element per wavelength (when an element is larger than an acoustic wavelength!).

The convergence of the method for an incident vorticity wave is shown in Fig. 7. As for the acoustic wave, the rate of convergence increases with the number of plane waves. By inspection of the numerical results it was found that the rate of convergence is given by $N_h - 1$. With 9 plane waves, the error is below 1% with just 0.7 element per wavelength or 3 degrees of freedom per wavelength (note that in Fig. 7 the wavelength is the hydrodynamic wavelength given by $2\pi\mathbf{v}_0 \cdot \boldsymbol{\theta}/\omega$).

4.3. Conditioning

Wave-based numerical methods, such as PUFEM, UWVF and DEM, are known to suffer from a poor conditioning. But the extent of the ill-conditioning varies for each method. For instance the discontinuous Galerkin method with Lagrange multipliers for the Helmholtz equation is known to exhibit a better conditioning than the partition of unity method [12]. Also the ultra-weak variational formulation was found to be better conditioned than the partition of unity and than the least square methods for Helmholtz problem [37].

Fig. 8 shows the condition number of the linear system for an acoustic incident wave with various numbers of acoustic waves (note however that the condition number is independent of the nature of the incident wave as it has no influence on the left-hand side of the algebraic equations). The condition number is plotted against the number of elements per wavelength and the accuracy. The corresponding results for an incident vorticity waves are shown in Fig. 9. It is observed that the growth rate of the condition number with the number of elements per wavelength increases with the number of plane waves in the basis. With a large number of plane waves, the condition number can quickly reach values as high as 10^{15}. However, the situation is not as bleak as it seems if one considers the condition number plotted against the relative error. It is observed that severely ill-conditioned systems are only obtained for very high levels of accuracy with the relative error being approximately 10^{-5} or 10^{-6}. Such a level of precision is generally excessive for practical calculations (for engineering

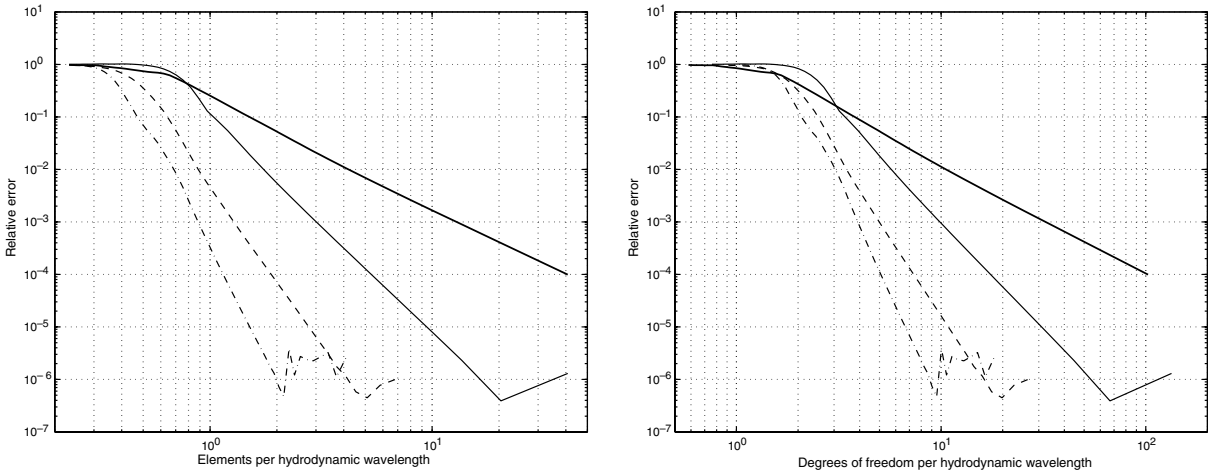

Fig. 7. Convergence for an incident vorticity waves with different number of vorticity plane waves in the basis. Relative error plotted against the number of elements per hydrodynamic wavelength (left) and against the number of degrees of freedom per hydrodynamic wavelength (right). $N_h = 3$ (thick solid line), $N_h = 5$ (thin solid line), $N_h = 7$ (thin dashed line), $N_h = 9$ (thin dot–dashed line).

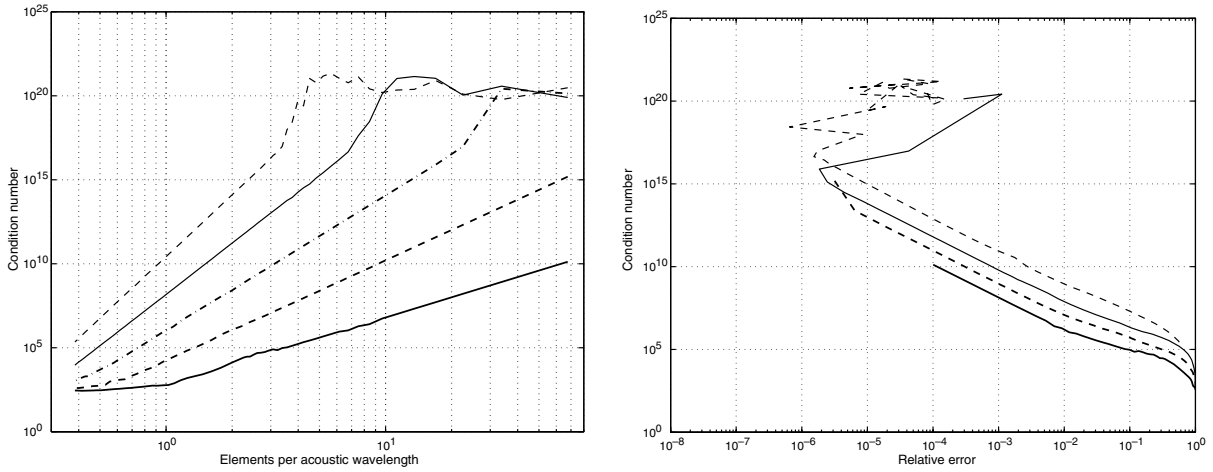

Fig. 8. Condition number versus the number of element per acoustic wavelength (left) and versus the relative error (right) for an acoustic incident wave. The plane wave basis is composed of acoustic plane waves with $N_a = 6$ (thick solid line), $N_a = 8$ (thick dashed line), $N_a = 10$ (thin solid line), $N_a = 12$ (thin dashed line), $N_a = 14$ (thin dot–dashed line).

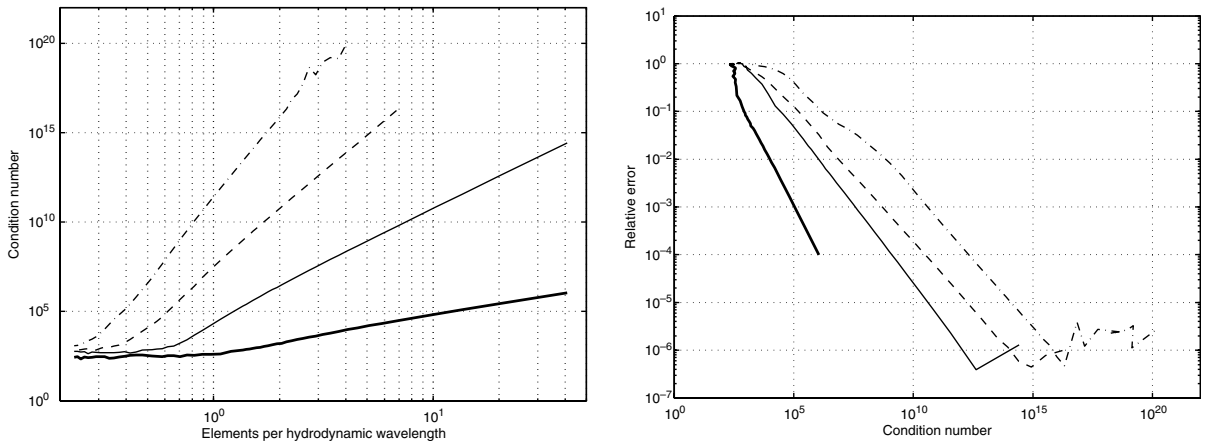

Fig. 9. Condition number versus the number of element per hydrodynamic wavelength (left) and versus the relative error (right) for an hydrodynamic incident wave. The plane wave basis is composed of acoustic plane waves with $N_h = 3$ (thick solid line), $N_h = 5$ (thin solid line), $N_h = 7$ (thin dashed line), $N_h = 9$ (thin dot–dashed line).

purposes a relative error of the order of 1% is acceptable). Therefore in practice the conditioning of the method is not critical.

These results clearly show that it is crucial to choose carefully the number of plane waves in order to control the conditioning of the numerical model. Huttunen et al. devised an automated technique to choose the optimal number of plane waves in each element so as to achieve a given condition number [18]. For instance, for a mesh with a varying element size, this method will automatically allocate more plane waves to large elements in order to accommodate for the reduced mesh resolution. It should be possible to adapt such a technique to the discontinuous Galerkin method with plane waves, but this will not be pursued in the present paper.

Moreover it is possible to use pre-conditioners to improve the conditioning before solving the linear system. A variety of pre-conditioning techniques have been developed and their performances can be quite dependent on the particular problem at hand. For the UWVF for Helmholtz problems, Huttunen et al. have successfully used a simple pre-conditioner [18]. The pre-conditioning matrix is block-diagonal with each block being copied from the corresponding block in the global matrix. The inverse of the pre-conditioning matrix can be easily computed by inverting each block separately and does not represent a significant overhead. To demonstrate that

such a pre-conditioner can also be applied with the present numerical method, Fig. 10 shows the condition number of the global matrix before and after pre-conditioning both for acoustic waves and hydrodynamic waves. It is clear that this simple pre-conditioner can reduce the condition number by several orders of magnitude and that it can efficiently mitigate the conditioning issue of the wave-based discontinuous Galerkin methods.

4.4. Comparisons with finite difference schemes

In order to put the performance of the present numerical method in perspective with more standard computational techniques for aeroacoustics, it is compared against the dispersion-relation-preserving scheme which is a high-order finite difference method optimized to minimize the dispersion error in a range of wavenumber [26]. This is a very common method in computational aeroacoustics in particular to solve the linearized Euler equations in the time domain. We consider the same simple benchmark problem as above. A regular cartesian grid is used to discretize the computational domain for the finite difference solution. The spatial derivatives in the conservation Eq. (2) are approximated using the 7-point DRP schemes.

The non-homogeneous radiation and outflow boundary conditions developed by Tam et al. are used to generate the incoming plane wave inside the computational domain [38]. For the discontinuous Galerkin method, the mesh shown in Fig. 3 is used and the plane wave basis is composed of 12 acoustic waves and 7 vortical waves. A 38×38 grid is used for the DRP schemes so that the two numerical models have exactly the same number of degrees of freedom.

We first compare the anisotropy of the finite difference schemes with that of the wave-based discontinuous Galerkin method, see Fig. 11. It is clear that for all wave directions the numerical error of the finite difference solutions is at least one order of magnitude larger than that of the wave-based discontinuous Galerkin method (and two orders of magnitude larger in some cases). To fix ideas, for an incident acoustic wave with $\theta = 3\pi/4$ the DRP scheme has 7.4 points per wavelength and achieves an accuracy of 1.2%. With the wave-based discontinuous Galerkin method the numerical error is 0.03% with just 2 elements per wavelength. The results for the vorticity wave are also shown in Fig. 11. The wave-based DG method is invariably more accurate than the DRP scheme by at least one order of magnitude. It is interesting to note that the large numerical error already observed in Section 4.1 for hydrodynamic waves propagating at large angles from the mean flow is also observed with the finite-difference scheme.

Convergence results are shown in Fig. 12 with the same parameters as in Section 4.2. As for the discontinuous Galerkin method, the grid of the finite difference solutions remains unchanged and the frequency is varied. The finite difference scheme is found to be less efficient both for acoustic and vorticity waves. These results demonstrate clearly that, for a given number of degrees of freedom, the discontinuous Galerkin method outperforms the DRP finite difference scheme.

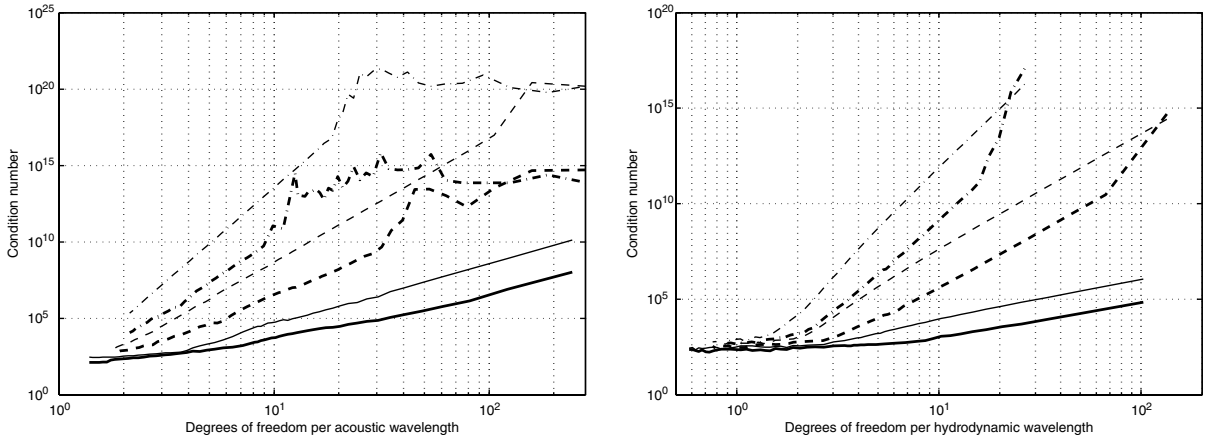

Fig. 10. Influence of the pre-conditioner for hydrodynamic waves (left) and acoustic waves (right). Thin lines: no pre-conditioner; Thick lines: with pre-conditioner. Left: $N_h = 3$ (solid line), $N_h = 5$ (dashed line), $N_h = 7$ (dot–dashed line). Right: $N_a = 6$ (solid line), $N_a = 10$ (dashed line), $N_a = 14$ (dot–dashed line).

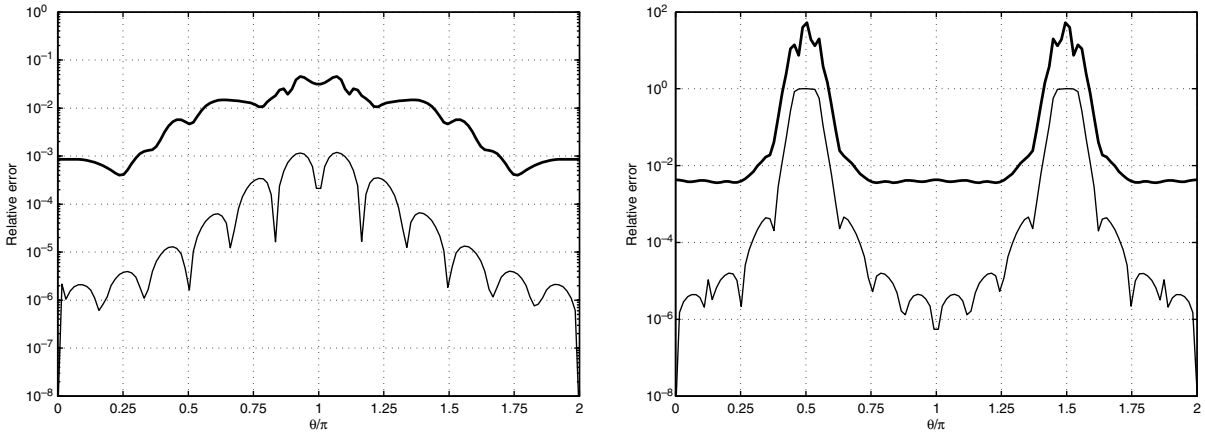

Fig. 11. Anisotropy of the present method and the finite difference scheme. Left: acoustic wave with $\omega = 20$; Right: hydrodynamic wave with $\omega = 10$. Thin lines: discontinuous Galerkin method with $N_a = 12$ and $N_h = 7$. Thick lines: DRP scheme with a 38×38 grid.

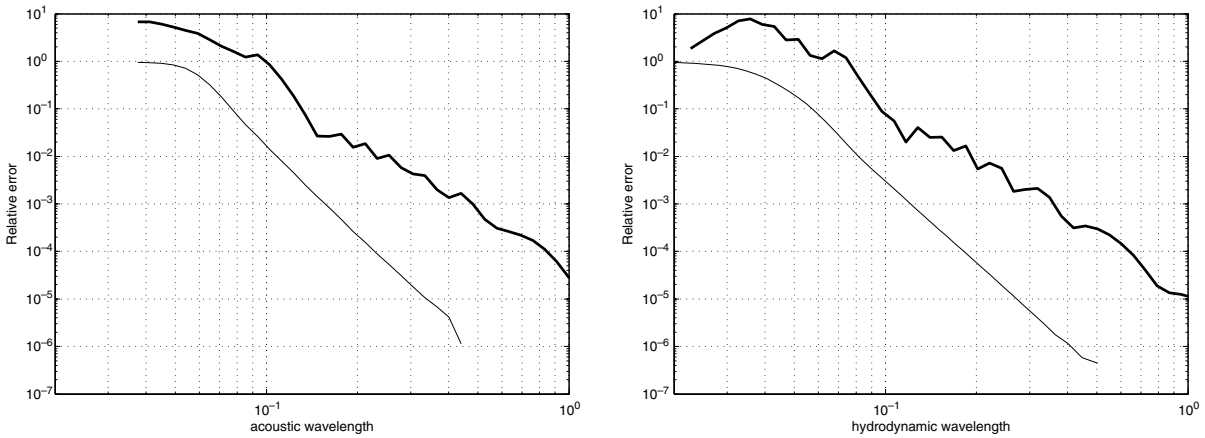

Fig. 12. Convergence of the present method and the finite difference scheme. Left: acoustic wave; Right: hydrodynamic wave. Thin lines: discontinuous Galerkin method with $N_a = 12$ and $N_h = 7$. Thick lines: DRP scheme with a 38×38 grid.

5. Source terms and singular solutions

In the present method, source terms are represented by the right-hand side **s** in (2). With wave-based methods a particular issue arises for non-homogeneous equations since the plane waves are solutions of the homogeneous problem and one might question the ability of the plane wave basis to describe the solutions when sources are present on the right-hand side of (2). For the partition of unity method, it was shown that in such cases the numerical model is robust but exhibits a low order of convergence as the mesh resolution is increased [8]. A first-order convergence is also observed for the ultra-weak variational formulation [16].

Furthermore, solving accurately Eq. (2) in the vicinity of a localized source can sometimes be difficult. Several sources of practical interest such as electromagnetic or acoustic monopoles and dipoles generate solutions that are singular and with large gradients in the region near the source. Although plane wave bases form a consistent approximation of singular functions (i.e. the error between the best approximation and the exact function decreases as the number of plane waves is increased), the convergence of the numerical method is not guaranteed when the exact solution is singular. This is due to the fact that Galerkin formulations do not necessarily yield the approximate solutions that minimize the numerical error. For more details on this aspect of wave-based numerical method, the reader is referred to [9,22,37]. A simple way to improve the numerical solution is to increase significantly the mesh resolution in the vicinity of the

source. As a consequence the number of plane waves per element in this region will be reduced in order to control the conditioning of the problem. This method was used with the ultra-weak variational formulation for Maxwell's equations by Huttunen et al. in [21, Fig. 2] where a very fine mesh was used to represent an electromagnetic dipole. However, the downside is that it inevitably increases significantly the problem size.

In an attempt to solve efficiently problems with point sources and singular solutions, a different method is devised in this section by modifying the variational formulation and removing explicitly the singular part of the solution.

5.1. Modified variational formulation

First we assume that the source $\mathbf{s}$ is contained within a particular element Ω_k (this is obviously the case for any point sources as they can be described by the Dirac function and its derivatives). The coefficients in the element Ω_k are uniform and we denote $\mathbf{u}_s$ the solution generated by the point source if it was in an infinite uniform medium with the same coefficients as inside the element Ω_k.

$$-\mathrm{i}\omega\mathbf{u}_s + \mathbf{A}_k\frac{\partial\mathbf{u}_s}{\partial x} + \mathbf{B}_k\frac{\partial\mathbf{u}_s}{\partial y} = \mathbf{s}, \quad \text{on } \mathbb{R}^2. \tag{28}$$

By using the trial function $\mathbf{v}_k$ for the element k the following weak variational formulation can be derived

$$\int_{\partial\Omega_k}\mathbf{v}_k^{\mathrm{T}}\mathbf{F}_k\mathbf{u}_s\mathrm{d}\Gamma = \int_{\Omega_k}\mathbf{v}_k^{\mathrm{T}}\mathbf{s}\mathrm{d}\Omega. \tag{29}$$

It is therefore possible to substitute the singular source term in the right-hand side of Eq. (2) by an equivalent flux across the contour of Ω_k.

We now have to remove the singularity of the solution. To that end, the solution $\mathbf{u}_k$ inside the element Ω_k is rewritten as $\mathbf{u}_k + \mathbf{u}_s$ so that $\mathbf{u}_k$ now represents the regular part of the solution in the element Ω_k, whereas for all the other elements it still denotes the total solution. After the substitution the variational formulation (22) of the problem reads

$$\sum_e\sum_{e'<e}\int_{\Gamma_{e,e'}}(\mathbf{v}_e-\mathbf{v}_{e'})^{\mathrm{T}}(\mathbf{F}^+_{e,e'}\mathbf{u}_e+\mathbf{F}^-_{e,e'}\mathbf{u}_{e'})\mathrm{d}\Gamma + \int_{\partial\Omega}\mathbf{v}^{\mathrm{T}}\mathbf{F}\mathbf{u}\mathrm{d}\Gamma = \sum_{e'<k}\int_{\Gamma_{k,e'}}\mathbf{v}_k^{\mathrm{T}}\mathbf{F}^-_{k,e'}\mathbf{u}_s + \mathbf{v}_{e'}^{\mathrm{T}}\mathbf{F}^+_{k,e'}\mathbf{u}_s\mathrm{d}\Gamma. \tag{30}$$

This is similar to formulation (22) except for the right-hand side where the original source term present inside the element Ω_k has been transformed into an equivalent source distributed along the edge of the element.

As the solution $\mathbf{u}_s$ is not a plane wave, the integral on the right-hand side cannot be evaluated in closed form and numerical integration schemes have to be used, such as Gauss quadratures. But it does not represent a significant overhead in computing time since it is only required for one element. This method can be readily modified if Ω_k is on the boundary of the computational domain.

5.2. Application to an acoustic point source with a uniform flow

To illustrate the efficiency of the modified variational formulation (30), we solve the problem of a point mass source embedded in a uniform flow where the source term in (2) is $\mathbf{s} = [1,0,0]^{\mathrm{T}}\delta(x-x_s)\delta(y-y_s)$. This problem is similar to the test cases used by Bailly and Juvé to benchmark finite difference methods for the linearized Euler equations in the time domain [39].

The exact solution $\mathbf{u}_s$ to Eq. (28) can be obtained in closed form and is given in [39]. The ambient sound speed and density are uniform, $c_0 = 1$, $\rho_0 = 1$. The mean flow is oriented in the positive x direction, with Mach number $M = 0.5$ so $u_0 = M$ and $v_0 = 0$. The angular frequency is $\omega = 40$. To represent the radiation of sound to the far field, ghost cells are used on the boundary of the computational domain with a zero solution outside the domain, i.e. $\mathbf{g} = 0$ in Eq. (27). To reduce spurious reflections at the boundary, the computational domain is circular with radius 1 and the point source is located at $x_s = -M$ and $y_s = 0$ so that the radiating waves hit the boundary at normal angle.

First, Fig. 14 illustrates the advantage of the modified formulation (30) over (5). While the original variational formulation is clearly unable to resolve even qualitatively the sound radiation from the point source, the solution based on the formulation (30) is quite accurate with the L_2-error on the pressure field being just 1%. It is noted that neither the mesh resolution nor the number of plane waves has been modified between the two results given in Fig. 14 (in both cases the element size is 0.08 and the plane wave basis is composed of 14 acoustic waves and 5 hydrodynamic waves).

To assess the influence of the mesh size and number of plane waves, three different mesh resolutions were considered (see Fig. 13) as well as a number of acoustic plane waves ranging from 8 to 14 (together with 5 vorticity waves). Shown in Fig. 15 are three examples of pressure profile along the x-axis. With the fine mesh and only 8 acoustic waves, the numerical solution is reasonably accurate in the downstream region where the acoustic wavelength is large but is unacceptable in the upstream direction where the acoustic wavelength is significantly shorter. With a coarse mesh but 14 acoustic plane waves results clearly improve although the amplitude is still slightly underestimated in the upstream region. And finally with the fine mesh and 14 acoustic plane waves the numerical solution is found to be very accurate.

Table 1 summarizes the L_2-error for pressure with the different combinations of mesh resolution and number of plane waves. As expected, the error decreases rapidly as the number of plane waves is increased. Comparatively, refining the mesh only yields limited improvement in accuracy. This is best illustrated by comparing the case of the fine mesh with 8 plane waves and the case of the coarse mesh with 14 plane waves. With less degrees of freedom the latter case achieves a much better accuracy with an error divided by 20. These results are in line with the conclusions drawn in Section 4.

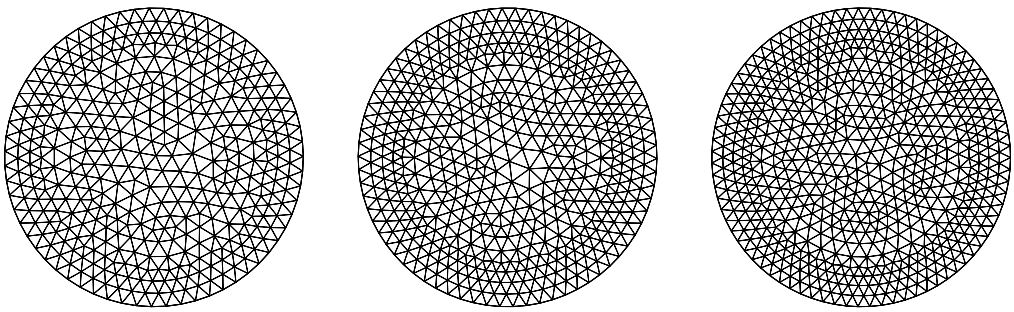

Fig. 13. Three triangular meshes with different resolutions. Left: element size 0.1, 765 elements; Center: element size 0.09, 980 elements; Right: element size 0.08, 1221 elements.

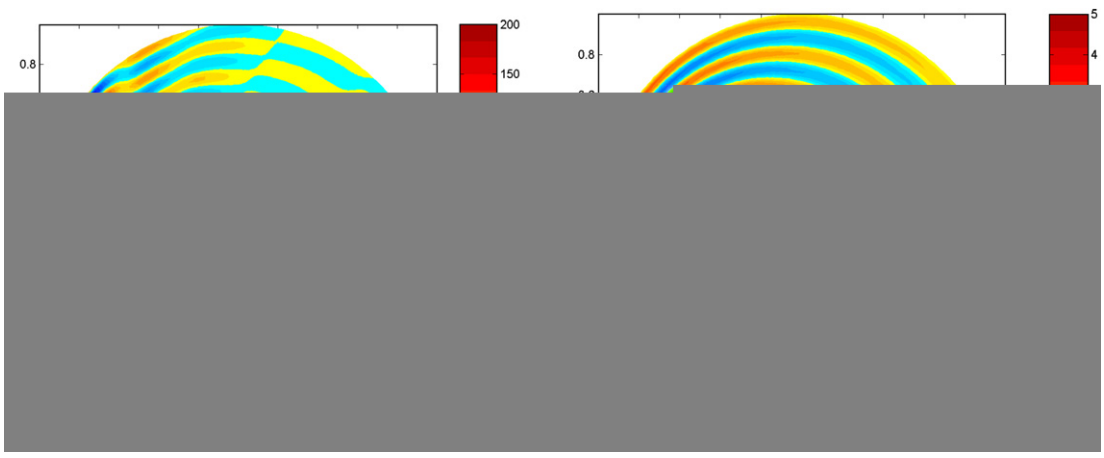

Fig. 14. Numerical solution for a point mass source in a uniform mean flow, with the standard formulation (22) (left) and with the modified formulation (30) (right).

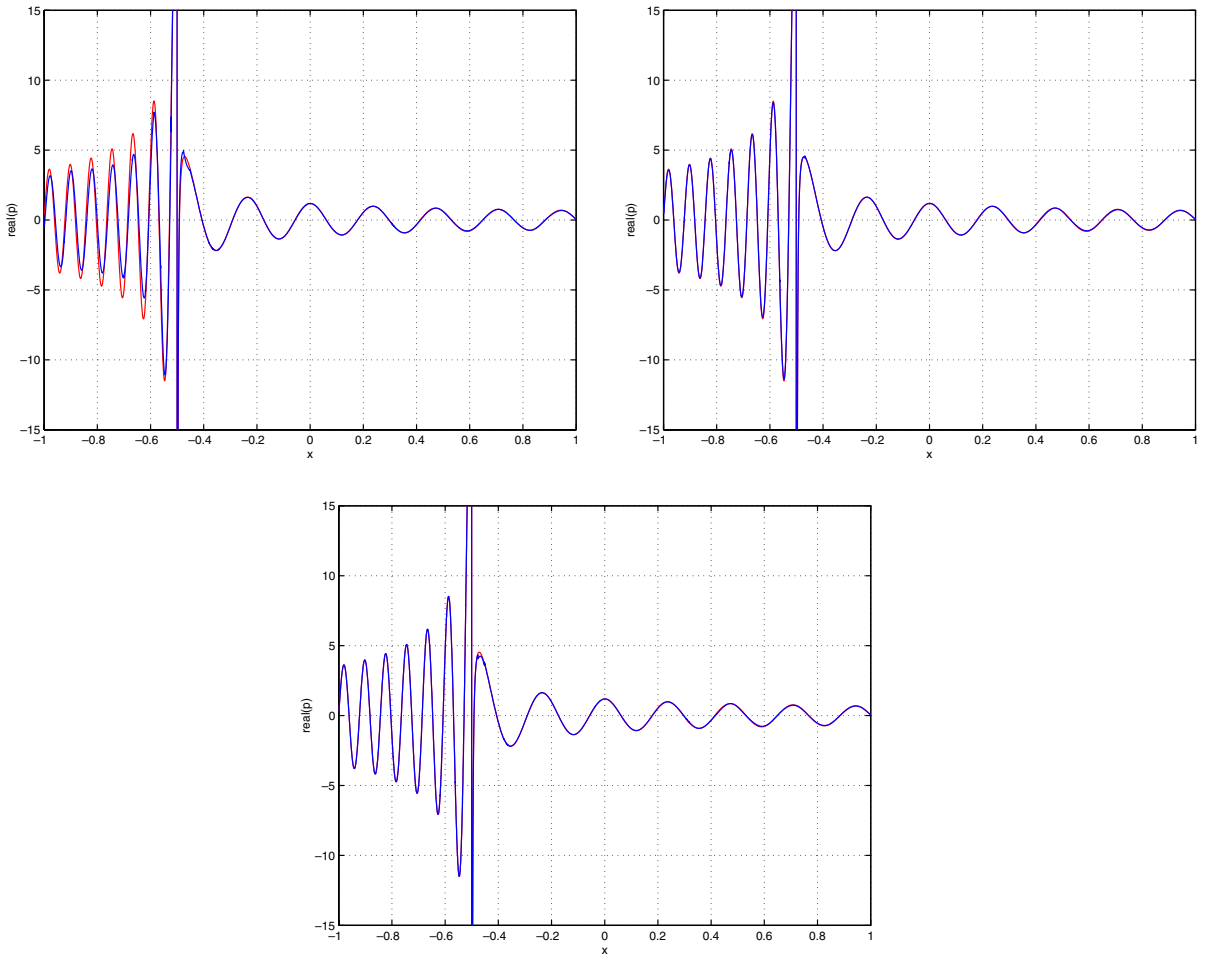

Fig. 15. Pressure profile along the x-axis with different mesh resolutions and number of plane waves. Top left: fine mesh with 8 plane waves; Top right: coarse mesh with 14 plane waves; Bottom: fine mesh with 14 plane waves. Exact solution (red), numerical solution (blue). (For interpretation of the references in colour in this figure legend, the reader is referred to the web version of this article.)

Table 1
L_2-error on pressure and number of degrees of freedom for the point mass source in a uniform flow with different mesh resolutions and numbers of acoustic plane waves

	Coarse mesh		Intermediate mesh		Fine mesh	
	Error (%)	n_{dof}	Error (%)	n_{dof}	Error (%)	n_{dof}
$N_a = 8$	46	9945	37	12740	31	15873
$N_a = 10$	18	11475	10.4	14700	7	18315
$N_a = 12$	4.4	13005	2.5	16660	1.7	20757
$N_a = 14$	1.5	14535	1.3	18620	1	23199

6. Application to non-uniform flows

We now consider a case where the base flow is not uniform by solving the problem of a point source embedded in a two-dimensional cold jet. The configuration is the same as in Section 5.2 except that the flow velocity has now a Gaussian profile

$$u_0(y) = u_\infty + (u_{jet} - u_\infty)\mathrm{e}^{-\log(2)(y/b)^2},$$

where b is the width of the jet, u_∞ is the free stream velocity and u_{jet} is the velocity on the centerline of the jet. Here we choose the parameters $u_\infty = 0.2$, $u_{jet} = 0.5$ and $b = 0.14$. The flow velocity profile is shown in Fig. 16. This test case is similar to the benchmark problem for computational aeroacoustics devised by Agarwal et al. [40] (although with different parameters).

For the numerical calculations, the fine mesh shown in Fig. 13 was used together with 14 acoustic waves and 5 vorticity waves in each element. Fig. 16 shows the numerical solution for the real part of pressure. The refraction of acoustic waves by the mean flow shear is clearly visible. The acoustic waves propagating inside the jet are refracted in the transverse direction and this results in a region downstream of the source where the sound amplitude is significantly smaller (this is the so-called 'cone of silence').

In Fig. 17, the numerical solution for pressure is compared against the analytical solution of Agarwal et al. [40] along the line $y = 0.5$. It is found that the numerical result is in good agreement with the analytical solution. The slight difference observed is thought to originate mainly from spurious reflections at the boundary of

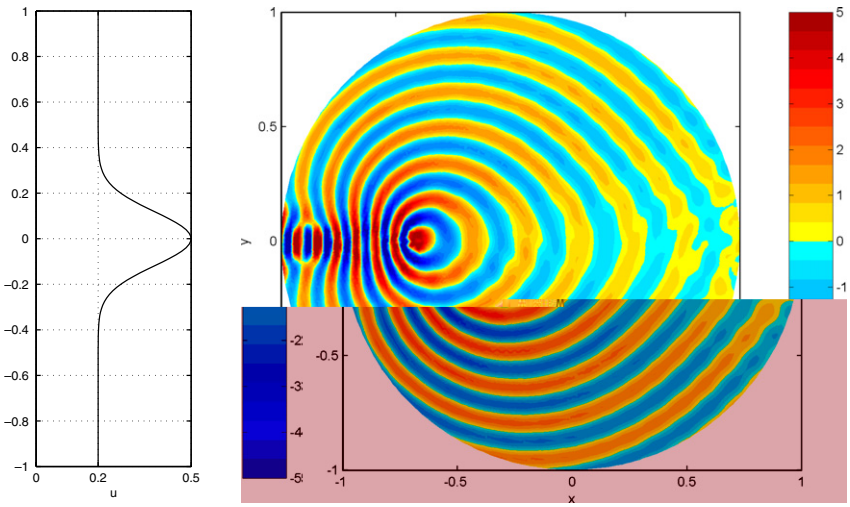

Fig. 16. Left: velocity profile of the jet. Right: real part of pressure for the noise radiated by a point source in a jet.

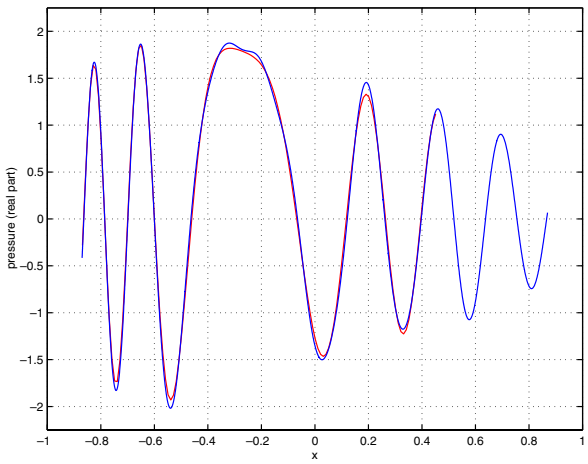

Fig. 17. Real part of pressure along the line $y = 0.5$. Red: theoretical solution; Blue: numerical solution. (For interpretation of the references in colour in this figure legend, the reader is referred to the web version of this article.)

the computational domain where ghost elements were used to implement a simple non-reflecting boundary condition. Although the use of ghost elements to remove spurious reflection is not optimal, it is sufficient to demonstrate that the present discontinuous Galerkin method is able to solve problems with non-uniform flows. The development of efficient non-reflecting boundary conditions for the physics-based DGM will surely improve the present results but this is beyond the scope of this paper.

Finally, it is worth noting that the results shown in Figs. 16 and 17 required approximately one minute on a standard desktop PC and less than 25000 degrees of freedom.

7. Conclusion

The general discontinuous Galerkin method presented in this paper relies on plane waves to approximate the solution instead of polynomials. This method can yield very accurate results even with a small number of degrees of freedom. The efficiency of this method stems from the fact that the dispersion relation of the continuous problem is used consistently throughout the formulation of the numerical scheme: it is used to define the plane wave basis for the solution and the trial function, it is also central to the formulation of the upwind flux splitting method.

This discontinuous Galerkin method was applied to the linearized Euler equations to solve aeroacoustic propagation problems. It can be applied to other linear wave propagation problems that can be formulated as a set of conservation equations of the form (2).

In the results presented here the number of plane waves was chosen manually and was the same for all the elements. To improve the efficiency and flexibility of the method it will be necessary to devise an automated procedure to define the number of plane waves based on the element size, the frequency and the parameters. Huttunen et al. have developed such a method for the ultra-weak variational formulation for the Helmholtz equation [18] whereby the number of plane waves is adjusted to keep the conditioning of the model below a prescribed level. Another important aspect to develop for the discontinuous Galerkin method with plane waves is the use of efficient non-reflecting boundary conditions. An extension to the isentropic linearized Euler equations is also possible and this will involve the use of entropy waves in addition to the acoustic and vorticity waves. Finally, the use of a constant interpolation for the coefficients of the equations introduces an additional source of error when solving problems with non-uniform coefficients. This source of error will be assessed in future work.

Acknowledgments

The author is grateful to Prof. Jeremy Astley and Dr. Pablo Gamallo for many helpful discussions in the course of this work. Dr. Anurag Agarwal kindly provided the computer program to evaluate the analytical solution used in Section 6.

References

[1] F. Ihlenburg, I. Babuška, Finite element solution to the helmholtz equation with high wave number – Part ii: The *h*–*p*-version of the fem, SIAM Journal of Numerical Analysis 34 (1) (1997) 315–358.
[2] P. Lesaint, P.-A. Raviart, Mathematical aspects of finite elements in partial differential equations, Academic Press, 1974, Chap. On a finite element method for solving the neutron transport equation.
[3] L. Yuang, C.-W. Shu, Discontinuous Galerkin method based on non-polynomial approximation spaces, Journal of Computational Physics 218 (2006) 295–323.
[4] D. Gottlieb, J. Hesthaven, Spectral methods for hyperbolic problems, Journal of Computational and Applied Mathematics 128 (2001) 83–131.
[5] J. Caruthers, J. French, G. Raviprakash, Green function discretization for numerical solution of the Helmholtz equation, Journal of Sound and Vibration 187 (4) (1995) 553–568.
[6] P. Di Francescantonio, D. Casalino, Green's function discretization scheme for sound propagation in nonuniform flows, AIAA Journal 37 (10) (1999) 1161–1172.
[7] J. Melenk, On generalized finite element methods, Ph.D. thesis, University of Maryland (1995).
[8] J. Melenk, I. Babuška, The partition of unity finite element method: Basic theory and applications, Computer Methods in Applied Mechanics and Engineering 139 (1996) 289–314.

[9] I. Babuška, J. Melenk, The partition of unity method, International Journal for Numerical Methods in Engineering 40 (1997) 727–758.
[10] C. Farhat, I. Harari, L. Franca, The discontinuous enrichment method, Computer Methods in Applied Mechanics and Engineering 190 (2001) 6455–6479.
[11] C. Farhat, I. Harari, U. Hetmaniuk, The discontinuous enrichment method for multiscale analysis, Computer Methods in Applied Mechanics and Engineering 192 (2003) 3195–3209.
[12] C. Farhat, I. Harari, U. Hetmaniuk, A discontinuous Galerkin method with lagrange multipliers for the solution of Helmholtz problems in the mid-frequency regime, Computer Methods in Applied Mechanics and Engineering 192 (2003) 1389–1419.
[13] C. Farhat, R. Tezaur, P. Weidemann-Goiran, Higher-order extensions of a discontinuous Galerkin method for mid-frequency Helmholtz problems, International Journal for Numerical Methods in Engineering 61 (2004) 1938–1956.
[14] B. Després, Sur une formulation variationnelle de type ultra-faible, Comptes Rendus De L Academie Des Sciences Paris 318 (1994) 939–944.
[15] O. Cessenat, Application d'une nouvelle formulation variationelle aux équations d'ondes harmoniques. Problèmes de Helmholtz 2D et de Maxwell 3D, Ph.D. thesis, Paris IX Dauphine (1996).
[16] O. Cessenat, B. Després, Application of an ultra weak variational formulation of elliptic pdes to the two-dimensional helmholtz problem, SIAM Journal in Numerical Analysis 35 (1998) 255–299.
[17] O. Cessenat, B. Després, Using plane waves as base functions for solving time harmonic equations with the ultra weak variational formulation, Journal of Computational Acoustics 11 (2003) 227–238.
[18] T. Huttunen, P. Monk, J. Kaipio, Computational aspects of the ultra weak variational formulation, Journal of Computational Physics 182 (2002) 27–46.
[19] T. Huttunen, P. Monk, F. Collino, J. Kaipio, The ultra-weak variational formulation for elastic wave problems, SIAM Journal in Scientific Computing 25 (5) (2004) 1717–1742.
[20] T. Huttunen, J. Kaipio, P. Monk, The perfectly matched layer for the ultra weak variational formulation of the 3d helmholtz equation, International Journal for Numerical Methods in Engineering 61 (2004) 1072–1092.
[21] T. Huttunen, M. Malinen, P. Monk, Solving maxwell's equation using the ultra weak variational formulation, Journal of Computational Physics 223 (2007) 731–758.
[22] P. Monk, D.-Q. Wang, A least-squares method for the helmholtz equation, Computer Methods in Applied Mechanics and Engineering 175 (1999) 121–136.
[23] G. Capdeville, A new category of hermitian upwind schemes for computational acoustics, Journal of Computational Physics 210 (2005) 133–170.
[24] G. Capdeville, A new category of hermitian upwind schemes for computational acoustics – ii. Two-dimensional aeroacoustics, Journal of Computational Physics 217 (2006) 530–562.
[25] S. Lele, Compact finite-difference schemes with spectral-like resolution, Journal of Computational Physics 103 (1992) 16–42.
[26] C. Tam, J. Webb, Dispersion-relation-preserving finite difference schemes for computational acoustics, Journal of Computational Physics 107 (1993) 262–281.
[27] D. Casalino, M. Roger, M. Jacob, Prediction of sound propagation in ducted potential flows using green's function discretization, AIAA Journal 42 (4) (2004) 736–744.
[28] R. Astley, P. Gamallo, Special short wave elements for flow acoustics, Computer Methods in Applied Mechanics and Engineering 194 (2005) 341–353.
[29] P. Gamallo, R. Astley, The partition of unity finite element method for short wave acoustic propagation on non-uniform potential flows, International Journal for Numerical Methods in Engineering 65 (2006) 425–444.
[30] E. Toro, Riemann solvers and numerical methods for fluid dynamics: a practical introduction, Springer, 1999.
[31] R. Leveque, Finite volume methods for hyperbolic problems, Cambridge University Press, 2002.
[32] P. Ortiz, E. Sanchez, An improved partition of unity finite element model for diffraction problems, International Journal for Numerical Methods in Engineering 50 (2001) 2727–2740.
[33] P. Bettess, J. Shirron, O. Laghrouche, B. Peseux, R. Sugimoto, J. Trevelyan, A numerical integration scheme for special finite elements for the Helmholtz equation, International Journal for Numerical Methods in Engineering 56 (2003) 531–552.
[34] G. Gabard, On discontinuous galerkin methods with plane waves for the displacement-based equation, International Journal for Numerical Methods in Engineering 66 (2006) 549–569.
[35] S. Pope, Turbulent flows, Cambridge University Press, 2000.
[36] C. Canuto, Spectral methods in fluid dynamics, Springer-Verlag, New-York, 1988.
[37] P. Gamallo, R. Astley, Trefftz-type methods and the ultra weak variational formulation for solving shortwave two-dimensional helmholtz problems, International Journal for Numerical Methods in Engineering, in press.
[38] C. Tam, J. Fang, K. Kurbatskii, Non-homogeneous radiation and outflow boundary conditions simulating incoming acoustic and vorticity waves for exterior computational aeroacoustics problems, International Journal for Numerical Methods in Fluids 26 (1998) 1107–1123.
[39] C. Bailly, D. Juvé, Numerical solution of acoustic propagation problems using linearized euler equations, AIAA Journal 38 (1) (2000) 22–29.
[40] A. Agarwal, P. Morris, R. Mani, Calculation of sound propagation in nonuniform flows: suppression of instability waves, AIAA Journal 42 (1) (2004) 80–88.